MEASUREMENT OF GALACTIC LOGARITHMIC SPIRAL ARM PITCH ANGLE USING TWO-DIMENSIONAL FAST FOURIER TRANSFORM DECOMPOSITION

Benjamin L. Davis
Arkansas Center for Space and Planetary Sciences, 202 Field House, University of Arkansas, Fayetteville, AR 72701, USA

Joel C. Berrier, Douglas W. Shields, Julia Kennefick, and Daniel Kennefick
Department of Physics, University of Arkansas, 835 West Dickson Street, Fayetteville, AR 72701, USA and Arkansas Center for Space and Planetary Sciences, 202 Field House, University of Arkansas, Fayetteville, AR 72701, USA

Marc S. Seigar
Department of Physics and Astronomy, University of Arkansas at Little Rock, 2801 South University Avenue, Little Rock, AR 72204, USA and Arkansas Center for Space and Planetary Sciences, 202 Field House, University of Arkansas, Fayetteville, AR 72701, USA

Claud H. S. Lacy
Department of Physics, University of Arkansas, 835 West Dickson Street, Fayetteville, AR 72701, USA and Arkansas Center for Space and Planetary Sciences, 202 Field House, University of Arkansas, Fayetteville, AR 72701, USA

Ivânio Puerari
Instituto Nacional de Astrofísica, Optica y Electrónica, Calle Luis Enrique Erro 1, 72840 Santa María Tonantzintla, Puebla, Mexico
Published in ApJS, 199, 33

ABSTRACT

A logarithmic spiral is a prominent feature appearing in a majority of observed galaxies. This feature has long been associated with the traditional Hubble classification scheme, but historical quotes of pitch angle of spiral galaxies have been almost exclusively qualitative. We have developed a methodology, utilizing two-dimensional fast Fourier transformations of images of spiral galaxies, in order to isolate and measure the pitch angles of their spiral arms. Our technique provides a quantitative way to measure this morphological feature. This will allow comparison of spiral galaxy pitch angle to other galactic parameters and test spiral arm genesis theories. In this work, we detail our image processing and analysis of spiral galaxy images and discuss the robustness of our analysis techniques.

Subject headings: galaxies: spiral; galaxies: structure; galaxies: fundamental parameters

1. INTRODUCTION

Approximately 60% of galaxies in the local Universe are spiral (Buta 1989). A considerable number of these spiral galaxies show Grand Design structure, where the spiral pattern is uniform and spans the entire disc of the galaxy. In these galaxies, the spiral pattern is often logarithmic in nature (Seigar & James 1998), and so their appearance is scale independent. The best geometric measure for logarithmic spirals is the pitch angle, and this can be measured for any galaxy in which spiral structure can be discerned, independently of the distance to the galaxy.

It is worth noting that spiral structure has been observed for over 150 years[1] with no clear standard for quantitative measurement having emerged, even though it correlates well with other important features of galaxies, such as central supermassive black hole (SMBH) mass (Seigar et al. 2008). Furthermore, spiral arm pitch angle could serve as a means to discriminate between rival theories for the formation of spiral structure in galactic discs. The aim of this paper is to present one such

method, based on a Two-Dimensional (2-D) Fast Fourier Transform (FFT) algorithm[2], which decomposes images into spirals of different pitch angles and numbers of arms.

A long-standing and quite successful theory of spiral structure in galaxies is the quasi-stationary density wave model (Lin & Shu 1964). As gas enters this density wave, it is compressed to a density at which stars can form (Roberts 1969; Shu et al. 1972). These star forming regions, along with stars and gas, conglomerate together into spiral arms in the disc regions of spiral galaxies, with star forming regions found on the leading edges of arms, and dust (in the form of dust lanes) seen on their trailing edges.

A recently formulated rival theory proposes that spiral arms are composed of identifiable groups of stars in highly eccentric and chaotic orbits, which originate near the ends of galactic bars. These orbits, though chaotic, keep the stars grouped in relatively narrow tubes known as manifolds, which are responsible for the observed spiral structure (Athanassoula et al. 2009b,a, 2010). According to this theory, galaxies with stronger bar poten-

---

[1] Spiral structure in galaxies was observed as early as 1845 (Lord Rosse's sketch of M51; Herschel 1859).

[2] This code is publicly available for use at http://dafix.uark.edu/~ages/downloads.html and http://astro.host.ualr.edu/2DFFT/.

tials should have more open spiral structure. In a recent study of 27 galaxies, Martínez-García (2012) found that $\approx 60\%$ of galaxies corroborate this theory and that galaxies in which the spiral arms maintain a logarithmic shape for azimuthal ranges greater than $70°$ seem to corroborate the predicted trend.

Spiral galaxies are classified into three main types of spiral structure: grand design, flocculent (Elmegreen 1981), and multi-armed. Grand design spirals are well-defined two-armed galaxies and theoretical efforts have naturally focused on explaining these very striking patterns. Flocculent spirals are less regular with sporadic spiral arm segments. It has been proposed that the origins of this kind of spiral are quite different from grand design spirals, the products of stochastic self-propagating star formation being acted upon by the differential rotation of the disc to create segments with the appearance of spiral arms (Seiden & Gerola 1982). Multi-arm spirals have distinct spiral arms, not necessarily symmetrically spaced. It is likely that they formed as a result of galaxy harassment (frequent high speed galaxy encounters within clusters; Moore et al. 1996). Spiral arm generation from external forces has been proposed to explain the genesis of multi-arm spiral structure in our own Milky Way (e.g., Purcell et al. 2011).

In general, logarithmic spirals are good approximations of the shape of galactic spiral arms (Seigar & James 1998). Logarithmic spirals are defined in polar coordinates as

$$r = r_0 e^{\theta \tan(\phi)} \qquad (1)$$

where r is the radius, θ is the central angle, r_0 is the initial radius when $\theta = 0°$, and $-90° \leq \phi \leq 90°$ is the pitch angle. The limits for the absolute value of the pitch angle are $0°$ and $90°$, which produce a circle and a line, respectively. Pitch angle is defined as the angle between the line tangent to a circle and the line tangent to a logarithmic spiral at a specified radius. Small pitch angle absolute values are associated with tightly wound spirals and high absolute values with loosely wound spirals. The sign of the pitch angle indicates the chirality of the spiral, with positive pitch angles indicating clockwise outward winding and negative pitch angles indicating counterclockwise outward winding (as seen from a given observer's position, i.e., above or below the galactic plane).

In this paper we present a method for determining reliable galactic spiral arm pitch angles. Given sufficient quality images, our software can reliably measure pitch angles by iterative 2-D FFT analyses. The paper is outlined as follows: §2 describes the observations of the images we use and our procedure to prepare those images for measurement through our software. §3 details the need for and the nature of our iterative adaptation to the FFT software, along with interpretation of its results. §4 discusses how we determine errors on our measured pitch angles. §5 describes our image analysis and related tools for further image refinement and evaluation. Finally, in §6 we present a discussion of our results and a few possible applications of the code.

2. OBSERVATIONS AND DATA ANALYSIS TECHNIQUES

The galaxy images we use in this paper (unless mentioned otherwise) come from the Carnegie-Irvine Galaxy Survey (CGS[3]; Ho et al. 2011). This is a statistically complete, magnitude-limited sample of 605 bright ($B_T < 12.9$ mag), Southern ($\delta < 0°$) galaxies observed using the SITe2k CCD camera (with a pixel scale of $0.259''\,\mathrm{pixel}^{-1}$) on the 2.5 m du Pont telescope at the Las Campanas Observatory in Chile. The overall quality of the images is high, both in terms of resolution (median seeing $\sim 1''$), field-of-view ($8.9' \times 8.9'$), and depth (median limiting surface brightness $\sim 27.5, 26.9, 26.4,$ and 25.3 mag arcsec^{-2} in the B, V, R, and I bands, respectively). All CGS images have been oriented to have up as North and left as East (before we subsequently rotate images for deprojection purposes). In this paper, we use a subset of galaxies from the CGS sample in order to test our methods. For images not included in the CGS sample, we use the NASA/IPAC Extragalactic Database (NED)[4] to acquire images.

2.1. Two-Dimensional Fast Fourier Transformations of Galaxy Images

A program called *2DFFT* (Saraiva Schroeder et al. 1994) accomplishes the 2-D FFT decomposition of images. *2DFFT* itself is an adaptation of the *FOURN* routine from *Numerical Recipes in C* (Press et al. 1989) that deals with CCD (charge-coupled device) images. The program is intended to analyze face-on or deprojected galaxy orientations. The decomposition is modeled on logarithmic spirals. As pointed out by Considere & Athanassoula (1988), this method does not assume that observed spiral structures are logarithmic. It only decomposes the observed distributions into a superposition of logarithmic spirals of different pitch angles and number of arms, which can be thought of as building blocks. This is analogous to the usual Fourier method of decomposing signals into a superposition of sinusoidal functions of different frequency. As per Puerari et al. (2000), the amplitude of each Fourier component is given by

$$A(p,m) = \frac{1}{D} \int_{-\pi}^{+\pi} \int_{r_{min}}^{r_{max}} I(u,\theta) e^{-i(m\theta+pu)} du\,d\theta \quad (2)$$

where $u \equiv \ln r$, r (radius) and θ (central angle) are in polar coordinates, r_{min} is the inner radius, r_{max} is the outer radius of the user-defined calculation annulus, and D is a normalization factor written as

$$D = \int_{-\pi}^{+\pi} \int_{r_{min}}^{r_{max}} I(u,\theta) du\,d\theta. \qquad (3)$$

$I(u,\theta)$ is the distribution of light of a given deprojected galaxy, in a (u,θ) plane, m represents the number of arms or harmonic modes, and p is the variable associated with the pitch angle (ϕ), defined by

$$\tan(\phi) = \frac{-m}{p_{max}} \qquad (4)$$

with p_{max} being the value of p with the highest amplitude for a given harmonic mode (see Figure 1). As currently defined, the code calculates Equation 2 for $0 \leq m \leq 6$.
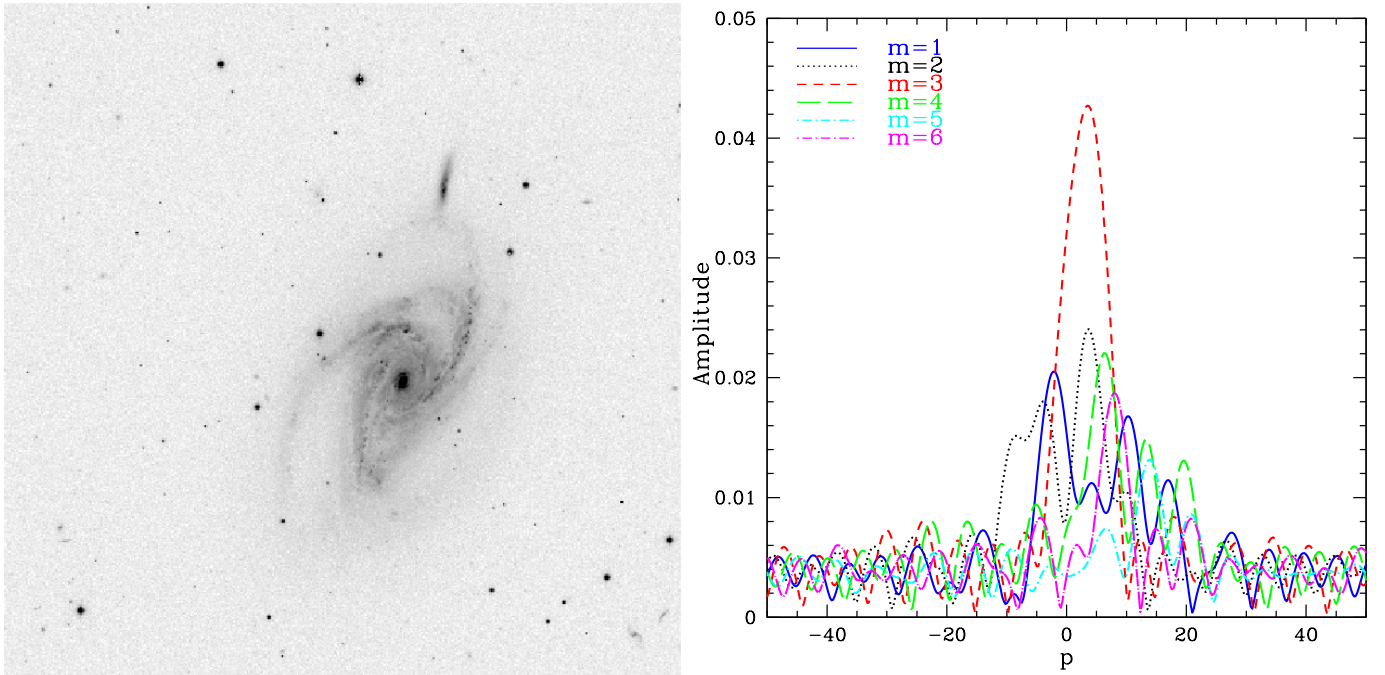

FIG. 1.— *Fig. 1a (left)* - B-band (inverted color) image of NGC 5054. NGC 5054 is measured to have a position angle (PA) of 160° and an inclination angle (α) of 53.84°. *Fig. 1b (right)* - $A(m, p)$ values for a deprojected B-band image of NGC 5054 with a measurement annulus defined by an inner radius of 160 pixels (41.4″) and an outer radius of 508 pixels (132″). This indicates a peak in the three-armed spiral harmonic mode at $p_{max} = 3.50$. The equivalent single value pitch angle via Equation 4 is $-40.60°$ (*Note* - subsequent sections and figures will revise this measurement with improved methods).

Additionally, the code reports a phase angle (Φ) for the orientation of the spiral arm pattern, calculated as

$$\Phi = arctan\frac{Im[A]}{Re[A]} \tag{5}$$

where $Im[A]$ and $Re[A]$ are the imaginary and the real part of $A(p, m)$, respectively.

2.2. *Image Preprocessing*

2.2.1. *Deprojection*

An important step in measuring the pitch angle of a galaxy, regardless of the method, is to deproject the galaxy to a face-on orientation. This process assumes that a galaxy with the plane of its disc parallel to the plane of the sky will be circular. A circular galaxy with random inclination appears on the sky as an ellipse. Thus, a circular galaxy can be described by its position angle (PA; orientation of the semi-major axis in degrees East of North) and its axis ratio. In turn, the axis ratio can be further incorporated to characterize the angle of inclination (α) from the plane of the sky defined by

$$\alpha = \arccos(b/a) \tag{6}$$

where a is the semi-major axis and b is the semi-minor axis. Thus, an inclination angle of 0° and 90° describes a face-on and an edge-on galaxy, respectively. The position angle and axis ratio can be determined easily from images using various programs, e.g., *SExtractor* (Source Extractor; Bertin & Arnouts 1996) or the *ELLIPSE* routine in IRAF[5] (Tody 1986; Jedrzejewski 1987). *ELLIPSE* works

by iteratively fitting isophotes interactively to a galaxy image and reporting various parameters; most importantly, position angle and ellipticity ($1 - (b/a)$).

With the position angle and axis ratio well-defined, the galaxy can be readily deprojected. This is accomplished by rotating the image of the galaxy (see Figure 2a) by $-PA$ (see Figure 2b) and then stretching the x-axis by the a/b axis ratio (see Figure 2c). We use the IRAF routines *ROTATE* and *MAGNIFY* to accomplish the image rotation and stretching, respectively. This procedure effectively aligns the semi-major axis of the galaxy with the y-axis on the image and then stretches the semi-minor axis to an equal length as the semi-major axis, thus creating one unique radius for the galaxy and turning what was an ellipse into a circle. The process of deprojection is conducted in order to minimize errors in the resulting measurement of pitch angle. However, as discussed later in §4.1, precise deprojection is not necessary for the measurement of the pitch angle. Deprojection increases the range of galactic radii over which valid pitch angles may be measured, and thus decreases error in those measurements. As a result, our assumption of galaxies being intrinsically circular is not especially critical to the measurement of spiral arm pitch angle. In the case of highly inclined (i.e., nearly edge-on) galaxies, much of the spiral arms are hidden from sight and recovery of the intrinsic geometry via deprojection becomes increasingly difficult with higher inclination angles. However, we have had success with deprojection on galaxies up to $\alpha = 77.47°$ for the case of IC 4831. Of course, the ability to ex-
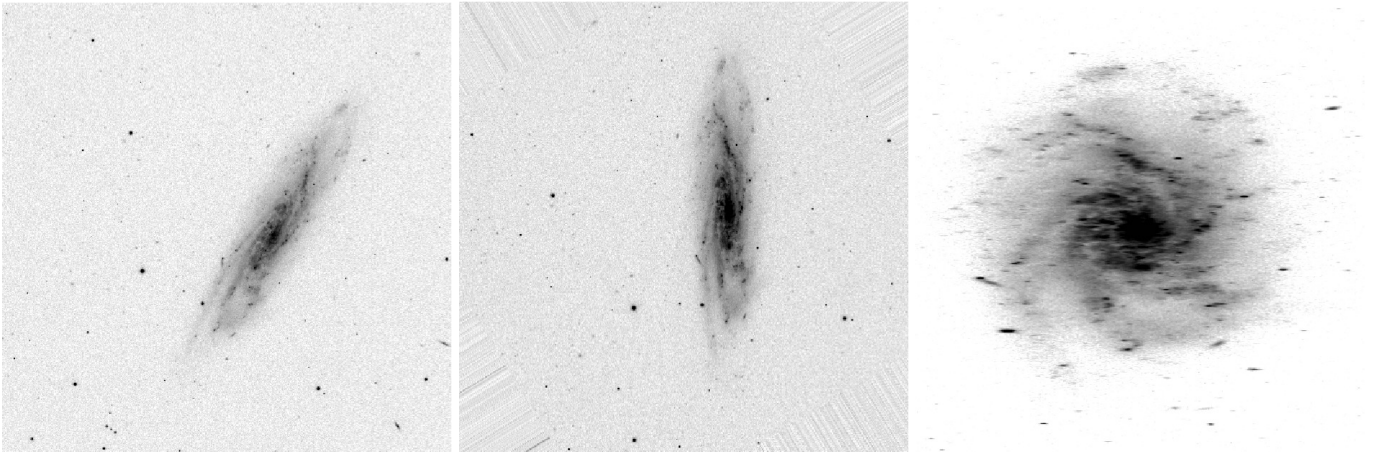
FIG. 2.— *Fig. 2a (left)* - B-band (inverted color) image of NGC 1337. NGC 1337 displays a position angle of $-30.97°$, a semi-minor to semi-major (b/a) axis ratio of 0.218, and a corresponding angle of inclination from the plane of the sky of $77.41°$ as determined by Equation 6. *Fig. 2b (middle)* - B-band (inverted color) image of NGC 1337 rotated by $30.97°$ $(-PA)$ to align the semi-major axis with the y-axis. *Fig. 2c (right)* - B-band (inverted color) image of NGC 1337: the result of stretching the x-axis of Fig. 2b by the a/b axis ratio (4.59), effectively deprojecting the image by circularizing the once elliptical shape of the galaxy. Subsequently, the image is cropped and made square with the center of the galaxy at the center of the image.

tract meaningful information from a deprojected image will strongly depend on the resolution of the image. For images of low to moderate resolution, it is unlikely to be able to meaningfully analyze galaxies with $\alpha > 60°$.

2.2.2. *Image Cropping*

After deprojection, the next step is to determine the center of the galaxy. We assume that the center of the galaxy is the brightest region within the galactic nucleus using the IRAF routine *IMCNTR* to determine the brightest pixel location within a specified search region. The apparent center of a galaxy is strongly affected by the interstellar extinction. As a result, different wavebands may yield slightly different center coordinates based on this routine. We have conducted a test of 10 randomly selected galaxies from the CGS sample and have determined that, on average, the positions of the central coordinates vary by a distance of 1.986 pixels $(0.514'')$ between B and I band images. This insignificant discrepancy is made even less important by further findings in §4.1, which show that measurement of pitch angle does not critically depend on location of the precise center of the galaxy. The *IMCNTR*-determined coordinates are then adopted as the center of the galaxy. The image is then cropped about the galaxy, with the center of the galaxy as the center of the cropped image (see Figure 2c), and the resulting image made to be a perfect square, as required by the *2DFFT* code, with odd-numbered pixel-sized edges in order to allow a unique median pixel location as the exact center of the image[6].

2.2.3. *Star Subtraction*

FFT image analysis is widely used for its mimicry of the human eye's ability to pick out symmetries and repetitions even in noisy or cluttered images. The *2DFFT* code can measure pitch angles, in spite of the presences of many non-spiral features in a galaxy's image. An interesting feature is that though the code models the spiral image as a superposition of spirals of different numbers of arms and different pitch angles, it measures the correct pitch angle even for harmonic modes where the number of spiral arms is incorrect. Thus, for a sufficiently low-noise image, it is not even necessary to correctly infer the number of spiral arms in the galaxy in order to accurately measure its pitch angle.

When noise is introduced, this agreement in pitch angle measurement between the different harmonic modes is the most obvious casualty. One important source of noise is the presence of bright foreground stars, especially when they are superimposed on the disc of the galaxy itself (see Figure 3). Nevertheless, the 2-D FFT of the harmonic mode with the correct number of arms (most commonly, $m = 2$) will still usually give a stable value, which seems to correspond to the correct pitch angle even when other harmonic modes show no reliable measure. In order to increase confidence in our pitch angle measurement, we reduce the noise by subtracting the foreground stars. Since the IRAF *ELLIPSE* function does not always work when analyzing star-subtracted images (it fails to start if light from the center of a galaxy has been removed and it cannot locate the center), it is best to measure the ellipticity before performing star subtraction[7]. Often, this results in several of the harmonic modes coming into at least rough agreement with the one harmonic mode previously selected as the best single example. This suggests that foreground star contamination is a leading source of noise in the images and that star subtraction is a useful step. At the same time, it may not always be required for an accurate measurement. This is corroborated by Martínez-García (2012), who finds from a study of 27 galaxies, that the presence of foreground stars does not affect the value of pitch angle in general.

---

[6] As required by the *2DFFT* code, the input image file must be in the form of a text file. We use the IRAF routine *WTEXT* to convert *.fits* images to *.txt* files.

[7] We fit a Gaussian Point Spread Function to the bright stars and subtract them using the IRAF package *DAOPHOT*.
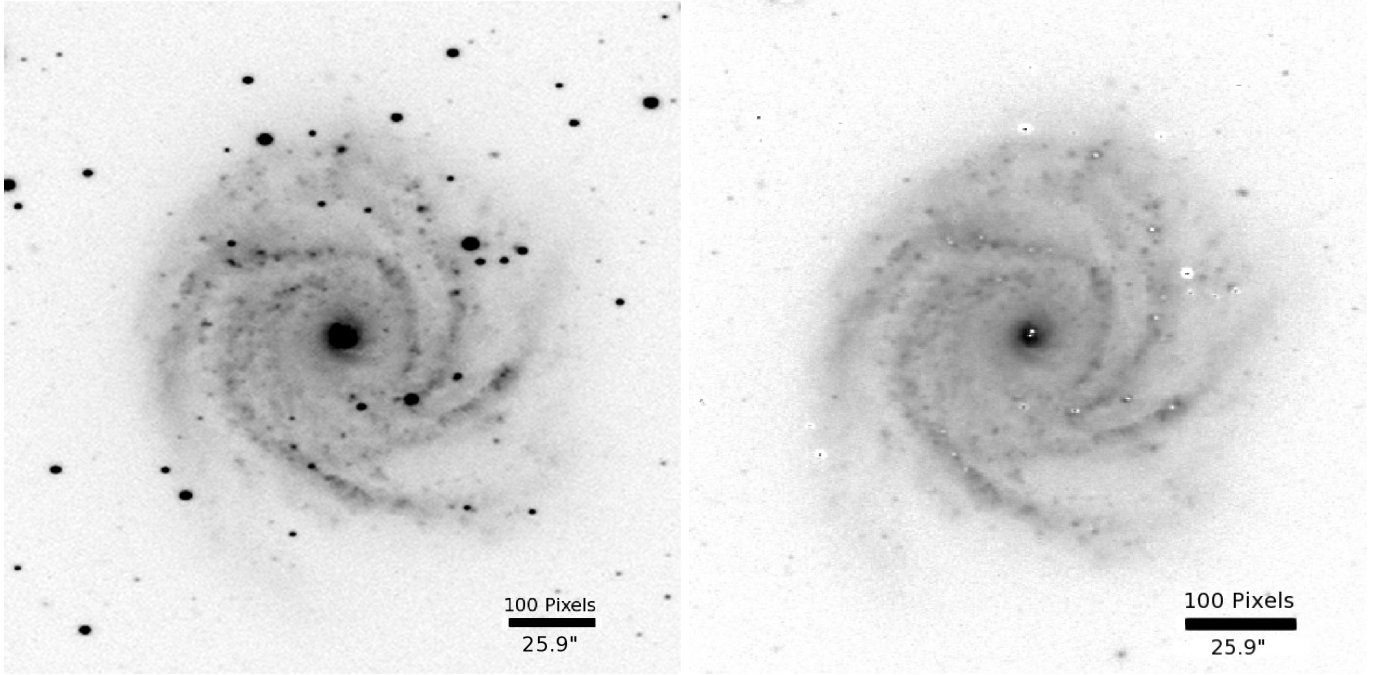
FIG. 3.— *Fig. 3a (left)* - Deprojected B-band image of IC 4538 before star subtraction. IC 4538 is measured to have $PA = 50°$ and $\alpha = 39.65°$. *Fig. 3b (right)* - Deprojected B-band (inverted color) image of IC 4538 after a Gaussian star subtraction was performed.

2.3. *Image Measurement*

Following pre-processing, the first step is to specify an inner and outer radius of the galactic disc. The inner radius is the location where the spiral arms begin, i.e., where the galactic bar or bulge terminates; the outer radius is the location where the spiral arms cease, usually the outermost visible radius of the galaxy. Thus, an annulus is defined within which the *2DFFT* code conducts its Fourier Decomposition. We then take this previously established procedure a step further by automating the code to measure many annuli so the final quoted pitch angle is not determined solely by one user-determined annulus. Our modifications and motivations behind the modifications to the code are detailed in the following section.

3. PITCH ANGLE AS A FUNCTION OF INNER RADII

The greatest source of human error lies in choosing an inner radius. Whereas it is seemingly easy for the user to visually identify the edge of the galaxy (i.e., the outer radius), it is significantly more difficult for the user to accurately specify the cessation of the bar/bulge feature of a galaxy (i.e., the inner radius). Furthermore, slight error in specification of the outer radius has little ill effect, whereas slight error in specification of the inner radius may have significant effect. To illustrate this result, consider different values in outer radii: underestimation results in the full length of spiral arms not being measured; overestimation results in the sky being measured at the edge of the spiral arms. Since our FFT computations are luminosity biased, sky inclusion does not significantly affect the computations. On the other hand, consider different values in inner radii: overestimation results in the full length of spiral arms not being measured; underestimation results in a bright bar/bulge feature being measured in addition to spiral arms, this

last case being the worst possible scenario.

As a result of this observed sensitivity to inner radius selection, we run *2DFFT* iteratively at different inner radii. This allows the user to specify an outer radius and calculate pitch angles for all possible inner radii within the defined outer radius. A scripting utility has been created to calculate pitch angles at all possible inner radii, given an outer radius, for a galaxy (see Figure 4). Additionally, we have modified the memory allocation of the original code to allow for input image sizes up to 2048×2048 pixels.

The inner radius is a numerical artifact which should not affect the measurement of pitch angle. Therefore, we seek a harmonic mode in which we find a range of inner radius over which the measured pitch angle appears to be the most stable and consistent with the observed appearance of the galaxy. We aim, typically, for a measurement of pitch angle with an associated error of 2° to 4°. The resulting pitch angles can be plotted vs. inner radius in order to visually identify stable pitch angle regions as a function of inner radius beyond the influence of a potential bar or oblate bulge feature. Stable regions are selected by several criteria; the stable region must be of the same sign (chirality) as the observed spiral arm windings in the image, it should be of the same harmonic mode as the visually observed number of spiral arms, there must not be any erratic fluctuation in pitch angle, and the region of stable pitch angles must be contiguous. In certain cases, the resultant pitch angle agrees in multiple harmonic modes, therefore, selection of the harmonic mode is not critically important. This allows us to focus on picking a stable pitch angle, even when the correct m value is ambiguous. To understand the code's behavior, we have conducted tests with very low noise images, artificially created logarithmic spirals. Not surprisingly, the code finds it trivial to measure the
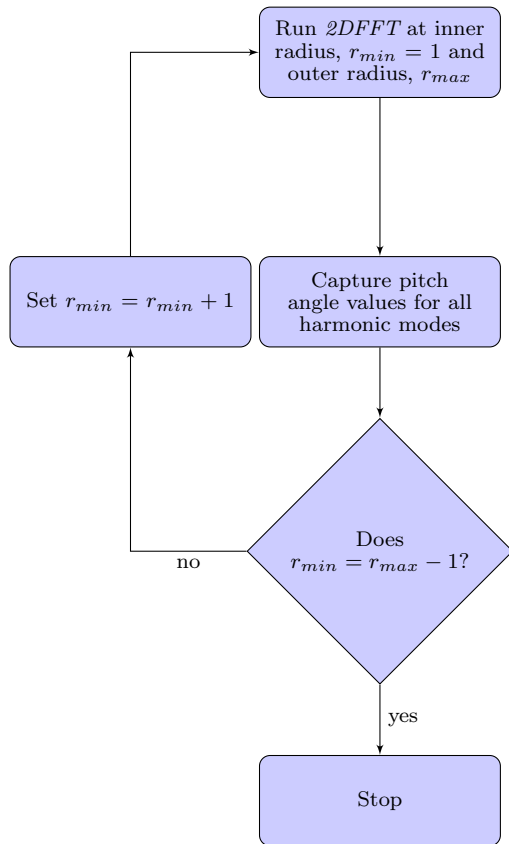
Fig. 4.— Flow chart representing our iterative method for measuring pitch angle as a function of inner radii.

pitch angle of such an image. For these synthetic spirals (see Figure 5), the apparent stable regions are easily perceptible. However, in real galaxies, careful image inspection and other techniques (see §5 and its subsections) are sometimes required to pick out more visually elusive stable regions amidst the range of harmonic modes available.

To be clear, our method does not avoid having to inspect each image individually. This is a necessary and not totally undesirable requirement. Computer vision methods are currently under development to measure galactic spiral arm pitch angle (e.g., Davis & Hayes 2012). The human eye has proven itself as the most reliable tool for the geometric classification of galaxies (e.g., Galaxy Zoo; Lintott et al. 2008). The human operator is required only to inspect the image qualitatively for signs of gross error, not to re-perform any measurements quantitatively.

An unavoidable side effect of deprojection is an oblate distortion of a galaxy's nuclear region. Initially, a nuclear galactic bulge is considered to be spheroidal. Therefore, a perfectly face-on galaxy (no deprojection required) with a nuclear bulge does not hinder the selection of an inner radius. This can be seen in the case of a synthetic logarithmic spiral with a nuclear bulge component added (see Figures 5c and 5g). Since a galaxy is deprojected according to the outer region of the galaxy and not the inner region, the nucleus can be distorted to an oblate spheroid. This creation of a non-spherically symmetric feature can negatively affect the calculated pitch angle

in the innermost regions of a galaxy.

The largest and likeliest source of error due to inner radii determination is when barred galaxies are measured. Galactic bars are linear features and therefore have high pitch angles ($\phi \simeq 90°$). Inclusion of a high pitch angle feature into the measurement annulus of the 2DFFT code results in a significant overall biasing of the resulting pitch angle towards the high side. This is always the case, because the highest practical limit for spiral arm pitch angle is significantly lower than the pitch angle produced by a galactic bar. The effect of galactic bars are illustrated in the example of a synthetic two-armed spiral with a bar component added (see Figures 5d and 5h).

4. ERROR DETERMINATION

The most obvious error is the variance about the mean pitch angle over the selected stable region in inner radii. The error is found by calculating the mean and standard deviation of the sample of pitch angles over the selected stable region. This standard deviation of pitch angle over the selected stable region is then weighted by the length of the stable region compared to the total length from the innermost spiral structure to the edge of the galaxy. Based on our observation from running synthetic logarithmic spirals through our code (see subsequent subsections), reliable pitch angles are not measurable for inner radii selected beyond $\approx 90\%$ of the selected outer radius. At this point, too much information has been ignored for the code to accurately measure a pitch angle.

In addition, it is important to consider the resolution of the 2DFFT code due to a discrete step size (see Figure 6). 2DFFT captures $-50 \leq p \leq 50$ values in discrete steps of 0.25 for six harmonic modes ($1 \leq m \leq 6$). Therefore, only discrete values of pitch angle are produced by the subsequent conversion of $p \rightarrow \phi$. The step size of the discrete Fourier transform is the analog of the frequency stepsize in One-Dimensional (1-D) discrete Fourier Transforms, the smallest measurable frequency. This leads to a necessarily higher precision in the lower regime of pitch angle absolute values and in the higher order harmonic modes. The quantized error of the mean pitch angle due to the resolution of the code (see Figure 7) is added in quadrature to the previously determined standard deviation of the mean pitch angle to give a total error. The final error is therefore

$$E_\phi = \sqrt{(\beta\sigma/\lambda)^2 + \epsilon_m^2} \qquad (7)$$

where E_ϕ is the total pitch angle error, ϵ_m is the quantized error for the dominant harmonic mode, σ is the standard deviation about the mean pitch angle, β is the distance (e.g., in pixels) from the innermost stable spiral structure (i.e., beyond the influence of a bulge or bar) to 90% of the selected outer radius of the galaxy ($0.9r_{max}$), and λ is the length (in the same units as used for β) of the stable range of radii over which the pitch angle is averaged. Figure 8 serves as a good example of our error determination and its subsequent reduction by the use of star subtraction.

Equation 7 reflects the fact that in our method, a human researcher rather than a computer makes the final selection of pitch angle. That is, a balance of two main principles governs Equation 7: the fluctuation across and
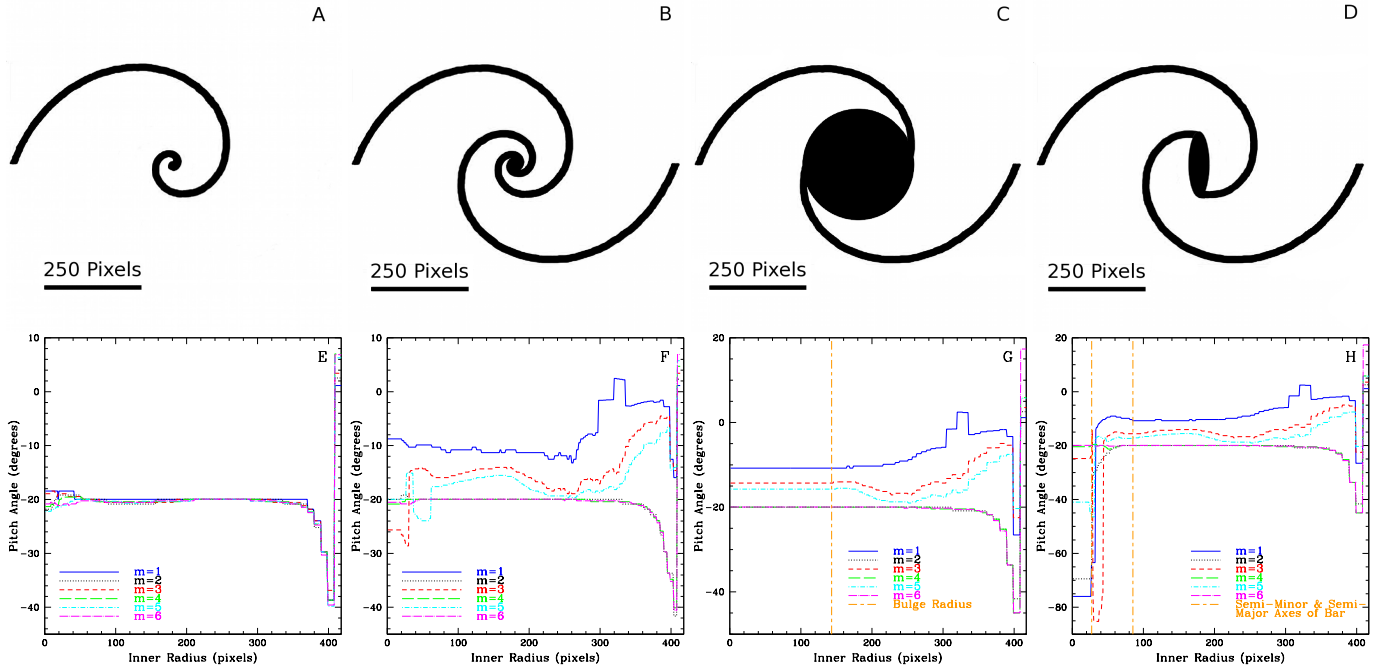
FIG. 5.— Synthetic spirals and their corresponding pitch angles as a function of inner radius below. The eight individual panels will be identified and discussed in the following top to bottom, left to right fashion. *Fig. 5a* - One-armed synthetic logarithmic spiral (inverted color) with $\phi = -20°$. *Fig. 5b* - Synthetic two-armed logarithmic spiral (inverted color) with a constant $m = 2$ pitch angle of $-20°$. *Fig. 5c* - $\phi = -20°$ synthetic two-armed logarithmic spiral (inverted color) with a circular bulge component added. *Fig. 5d* - $\phi = -20°$ synthetic two-armed logarithmic spiral (inverted color) with a barred nuclear component added. *Fig. 5e* - Pitch angle results for Fig. 5a. All harmonic modes display the correct pitch angle until $\approx 90\%$ of the outer radius is reached. *Fig. 5f* - Pitch angle results for Fig. 5b. The results for the even harmonic modes are essentially the same and accurately measure the correct pitch angle until $\approx 90\%$ of the outer radius is reached. *Fig. 5g* - Pitch angle results for Fig. 5c. The vertical line at 143 pixels represents the radius of the circular bulge. The odd numbered harmonic modes have a systematically lower absolute value of pitch angle, but the even harmonic modes are unchanged by the addition of a circular bulge component. *Fig. 5h* - Pitch angle results for Fig. 5d. The vertical lines at 27 and 85 pixels represent the semi-minor and semi-major axes of the bar, respectively. The odd numbered harmonic modes have systematically lower absolute values of pitch angle, just as in the case of the circular bulge component, but the innermost inner radii demonstrate intuitively high absolute values of pitch angle.
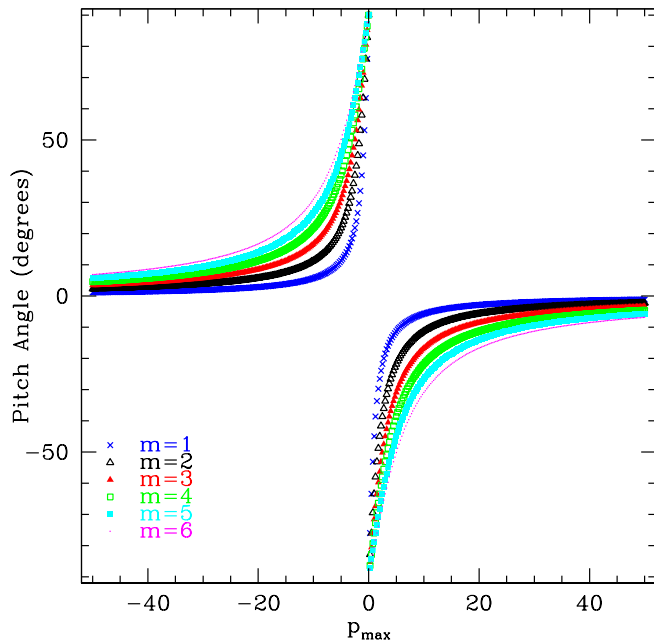

FIG. 6.— Every possible value of pitch angle calculable by the *2DFFT* code. Pitch angles are determined from p_{max} according to Equation 4.

the length of a chosen stable region of pitch angle as a function of inner radius. Our process ensures that the error about the mean pitch angle is appropriate, based on the choices made by the user. For example, an erratic "stable" region or a short stable region will both be punished with appropriately high errors. Thus, a careful selection of stable region is required so as not to produce substantial errors.

4.1. Inclination Angle and Galactic Center Position Errors

The problem of making a poor choice of inner radius was addressed by altering the code so that it calculates a pitch angle for all possible inner radii. Other user-defined parameters have little impact on our results, and thus do not require such measures. The most important step is deprojection, which requires the user to measure the galaxy's inclination angle, presuming that the galaxy's disc is inherently circular. Tests with a synthetic two-armed spiral with pitch angle of $-20°$ (see Figure 5b) demonstrate that measurement of pitch angle is correct for any even number of arms and for inner radii up to $\approx 90\%$ of the outer radius (see Figure 5f). For a one-armed synthetic spiral, all harmonic modes are in agreement (see Figure 5e).

When the synthetic two-armed spiral (see Figure 5b) is shrunk along one axis incrementally to simulate an in-
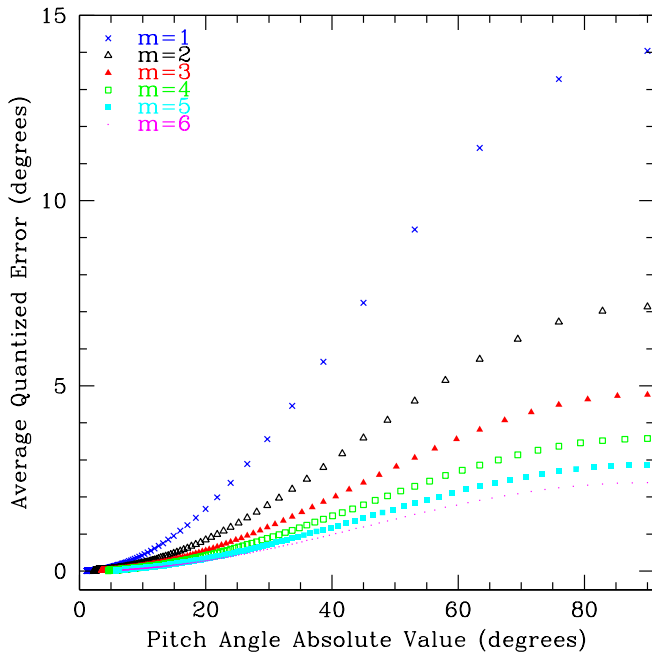
FIG. 7.— Every possible absolute value of pitch angle calculable by the *2DFFT* code and their resulting average quantized error due to the discrete step resolution. A third-ordered best fit polynomial is fit to each harmonic mode (m) to interpolate error values at all points: $y = -4 \times 10^{-5}x^3 + 0.0058x^2 - 0.0137x + 0.0234;$ $R^2 = 0.99994$ for $m = 1$, $y = -2 \times 10^{-5}x^3 + 0.0029x^2 - 0.0084x + 0.0222;$ $R^2 = 0.99997$ for $m = 2$, $y = -1 \times 10^{-5}x^3 + 0.002x^2 - 0.0064x + 0.0214;$ $R^2 = 0.99998$ for $m = 3$, $y = -1 \times 10^{-5}x^3 + 0.0015x^2 - 0.0054x + 0.0207;$ $R^2 = 0.99998$ for $m = 4$, $y = -9 \times 10^{-6}x^3 + 0.0012x^2 - 0.0046x + 0.02;$ $R^2 = 0.99999$ for $m = 5$, and $y = -7 \times 10^{-6}x^3 + 0.001x^2 - 0.0041x + 0.0191;$ $R^2 = 0.99999$ for $m = 6$.

creasingly inaccurate deprojection, the results show that there is still a stable region of inner radii with the correct measure of pitch angle (see Figure 9a). Similarly with a real two-armed galaxy, NGC 5247 (see Figure 10b), it is of interest that an incorrect choice of inclination angle merely causes a gradual reduction in the length of the stable region over which the selected inner radii yield the correct pitch angle (see Figure 9b). Thus, deprojection is still an important step, but is unlikely to be a significant source of error when using the script, which calculates pitch angle for a wide variety of possible inner radii.

Similarly, when choosing the center of the galaxy image, tests with a synthetic two-armed spiral (see Figure 5b) and a real two-armed galaxy (NGC 5247, see Figure 10b) suggest that incremental errors in centering only gradually reduce the stable region without affecting the actual measure of pitch angle (provided the stable region of roughly constant pitch angle remains lengthy enough to be found, see Figure 11). Overall, these tests are a testament to the robustness of the *2DFFT* algorithm.

4.2. *Bulges and Bars*

Our synthetic two-armed spiral was also used to study the effects of circular bulges and bars in galactic nuclei on pitch angle measurements. When a circular bulge component is added to the synthetic two-armed spiral (see Figure 5c), the even numbered harmonic modes are unaffected, whereas the odd harmonic modes are systematically different with the lower harmonic modes being

the worst (see Figure 5g). In contrast, when a bar component is added to the synthetic two-armed spiral (see Figure 5d), the resulting value of the measured pitch angle is significantly increased at inner radii, with the correct pitch angle value returning after the inner radius is beyond the extent of the bar (see Figure 5h). As an example, NGC 1365 (see Figure 12) displays a similar bar to the two-armed synthetic spiral with a bar added. These results confirm that circular bulges should not affect pitch angle, whereas the barred geometry can significantly bias pitch angle measurements towards higher values. We are therefore confident in the necessity of our efforts to systematically exclude barred nuclei from the pitch angle measurement annulus.

4.3. *Problems with Underlying Presumptions*

So far we have presumed that the pitch angle of a logarithmic spiral is a meaningful quantity to measure in images of disc galaxies. Certainly there are very many disc galaxies for which logarithmic spiral patterns are the most obvious feature of the disc, as the human eye perceives it. Nevertheless, two important objections might be made concerning the measurement of pitch angles as a useful characteristic of galaxies. One is that the pitch angle may be different for the same galaxy when viewed at different wavelengths. The other is that the pitch angle might vary with the radius of the disc, in other words that the spiral is not truly logarithmic.

4.3.1. *The Effect of Wavelength on Pitch Angle*

It is important to consider the possibility of different pitch angles arising in different wavebands of light and what physical processes that might imply. For instance, optical B-band images tend to trace the bright massive star forming regions of a galaxy and near-infrared (NIR) images tend to trace the old stellar populations in galaxies (Seigar & James 1998; Eskridge et al. 2002). The old stellar population traces the spiral density wave (Seigar & James 1998). Furthermore, a spiral that appears flocculent in the B-band may appear to have a weak grand design spiral in the near-infrared (Thornley 1996).

Kendall et al. (2011) used a 1-D FFT analysis on optical and NIR images of grand design spiral galaxies to measure their $m = 2$ pitch angles and concluded that a good correlation exists between galaxies being grand design in the infrared and in the optical. Seigar et al. (2006) demonstrates that a 1:1 relation exists between the B and NIR band pitch angles for a sample of 66 galaxies from a combination of the CGS (Ho et al. 2011) and the Ohio State University Bright Spiral Galaxy Survey (OSUBSGS; Eskridge et al. 2002). Alternatively, Grosbol & Patsis (1998) propose a contrary view. They find a systematic trend of arms being tighter in bluer colors by investigating five galaxies in B, V, I, and K' filters. Admittedly, two of their five galaxies are tight spirals for which little or no change in pitch angle is observed, but it seems that more work with multiple filters is required.

Using our method, we have remeasured a subset of 47 of the galaxies appearing in Seigar et al. (2006, they used an earlier version of this method) and have also identified a seemingly 1:1 relation (see Figure 13 and Table 1). Therefore, despite seemingly small-scale differences between spiral arms in different wavelengths of the optical-NIR spectrum, the overall structure of the spiral arms,
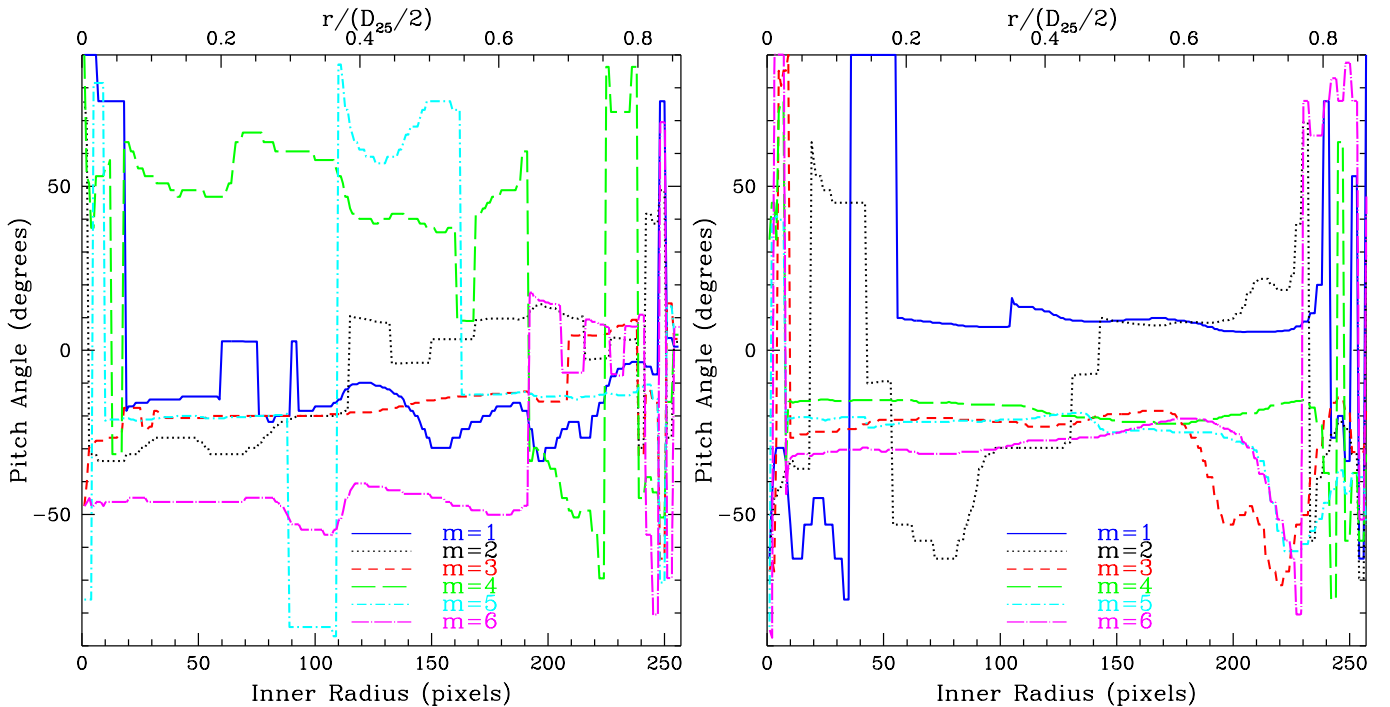
FIG. 8.— IC 4538 B-band pitch angle as a function of inner radius for deprojected ($PA = 50°$ & $\alpha = 39.65°$) images before (left) and after (right) Gaussian star subtraction was performed. $r/(D_{25}/2)$ is plotted on the secondary x-axis with D_{25} (major axis at the 25.0 B-mag/sq arcsec isophote) from the Third Reference Catalogue of Bright Galaxies (RC3; de Vaucouleurs et al. 1991). *Fig. 8a (left)* - a stable mean pitch angle of $-17.52°$ is determined for the $m = 3$ harmonic mode from a minimum inner radius of 36 pixels ($9.32''$) to a maximum inner radius of 208 pixels ($53.9''$), with an outer radius of 258 pixels ($66.8''$). This stable region of 172 pixels ($44.5''$) occupies 67% of the galactic disc. Equation 7 yields $E_\phi = 3.17°$ with $\lambda = 172$ pixels ($44.5''$), $\beta = 196$ pixels ($50.8''$), $\sigma = 2.75°$, and $\epsilon_3 = 0.47°$. The final determination of pitch angle is therefore $-17.52° \pm 3.17°$. *Fig. 8b (right)* - a stable mean pitch angle of $-17.98°$ is determined for the $m = 4$ harmonic mode from a minimum inner radius of 9 pixels ($2.33''$) to a maximum inner radius of 235 pixels ($60.9''$), with an outer radius of 264 pixels ($68.4''$). This stable region of 226 pixels ($58.5''$) occupies 86% of the galactic disc. Equation 7 yields $E_\phi = 2.61°$ with $\lambda = 226$ pixels ($58.5''$), $\beta = 229$ pixels ($59.3''$), $\sigma = 2.56°$, and $\epsilon_4 = 0.35°$. The final determination of pitch angle is therefore $-17.98° \pm 2.61°$. This result is barely different from the result without star subtraction; the main difference is the redetermination of the dominant harmonic mode. The percent difference in mean pitch angle is 2.59% with a 17.67% reduction in error from the original.

and thus the proposed density wave, is consistent across the optical-NIR spectrum. This is in opposition to the prediction of the density wave theory that different pitch angles are expected for spirals when observed in different bands (Hozumi 2003). Although, the expected difference in pitch angle across wavelength is probably small enough that an extremely high precision fit would be necessary to falsify this prediction of density wave theory.

From our experience, we have become accustomed to preferring B-band images in general due to their characteristic clarity of galactic stellar components. However, our comparison of pitch angles in different wavebands has convinced us that we can typically measure pitch angle across a wide range of electromagnetic wavelengths. In that regard, we have successfully measured pitch angles of galaxies in the extreme cases of far-ultraviolet and 21 cm radio wavelength images when no other imaging data was available.

4.3.2. *Variable Pitch Angle with Galactic Radius*

Occasionally, spiral arms may appear to change pitch angle in the outer region of the disc, sometimes discontinuously. These are more the exception than the rule and we have generally preferred to measure the inner part of the disc in such cases or use more elaborate processing methods (see §5.1) to mitigate the severity of pitch angle variability. Considering the case where a dichotomy ex-

ists between the pitch angles measured in the inner and outer regions of a galactic disc, the code can be made to run iteratively for two separate regions of the galaxy and average the results to yield an average pitch angle for the disc. However, if the pitch angle results are subsequently used for building relationships to processes in the nucleus of a galaxy (e.g., Seigar et al. 2008), pitch angles for the innermost portion of a galaxy perhaps make the most physical sense and are furthermore not as susceptible to extragalactic interaction. It is also likely that the entire extent of a galaxy might not display logarithmic spirals. If so, our stable regions are selected to only highlight clearly logarithmic sections of spiral arms.

To illustrate the case of measuring pitch angles of interacting galaxies, we have selected perhaps the most famous case of interacting galaxies, M51 (see Figure 14a). M51 consists of M51a (NGC 5194) and its companion dwarf galaxy M51b (NGC 5195). Due to M51a's clear interaction with M51b, its well-defined spiral structure is seen to depart from regularity close to the companion. For this case, our typical method of measuring pitch angle across the entirety of the galactic disc knowingly samples the outer 40% of the galaxy, which is clearly seen to be disrupted (see Figure 14b). Just as in the case of iterative determination of pitch angle as a function of inner radius to omit interior regions, by alternatively selecting
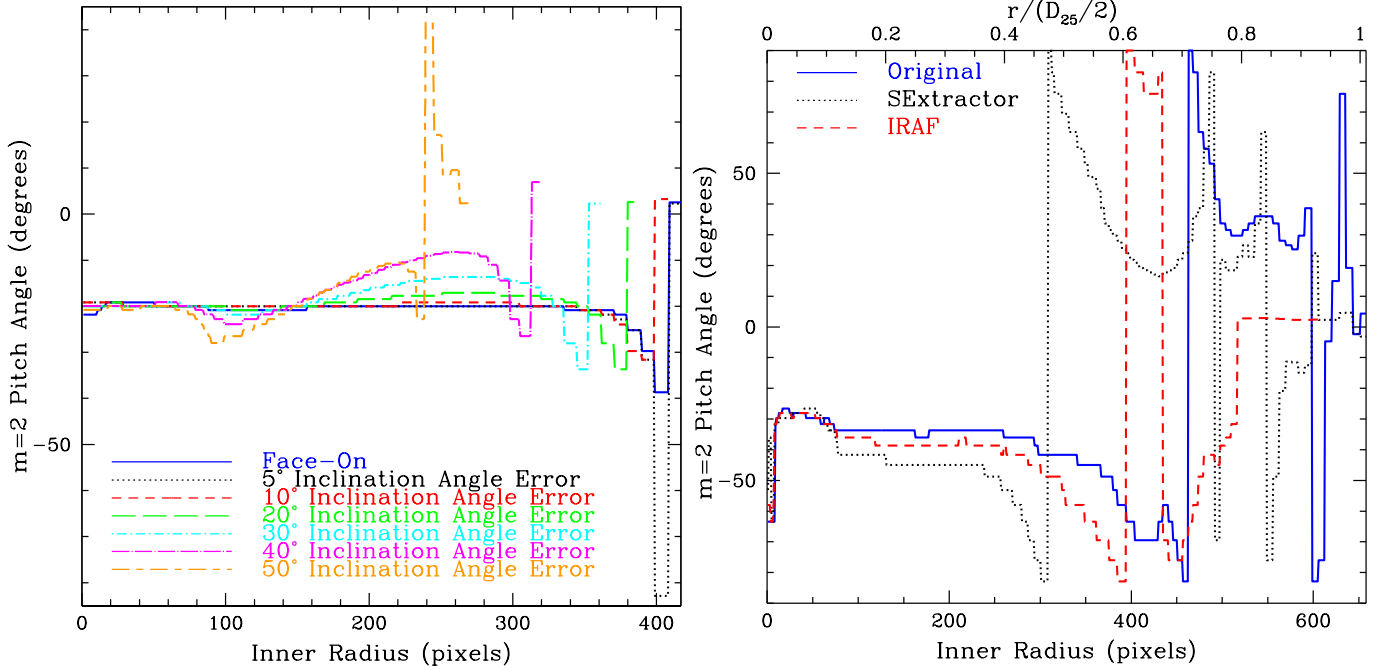
FIG. 9.— Inclination angle tests on pitch angle output for a synthetic two-armed logarithmic spiral (left) and a real two-armed galaxy (right). *Fig. 9a (left)* - Pitch angle results for different errors in inclination angle for the synthetic two-armed spiral in Fig. 5b. Even at a high degree of simulated inclination angle error, the mean pitch angles remain approximately the same despite a gradually shrinking stable region across inner radii. *Fig. 9b (right)* - Real two-armed galaxy inclination test using NGC 5247 (see Fig. 10b). Three angles of inclination are tested: Original - the galaxy before deprojection, *SExtractor* - incorporates the deprojection according to *SExtractor* ($PA = 30.4°$; $\alpha = 36.97°$), and IRAF - incorporates the deprojection according to IRAF ($PA = 38.71°$; $\alpha = 25.18°$). Pitch angle results over their respective stable regions are within each other's error bars. I-band pitch angle results are - Original: $-37.6° \pm 5.69°$, *SExtractor*: $-35.62° \pm 10.96°$, and IRAF: $-36.16° \pm 9.25°$.
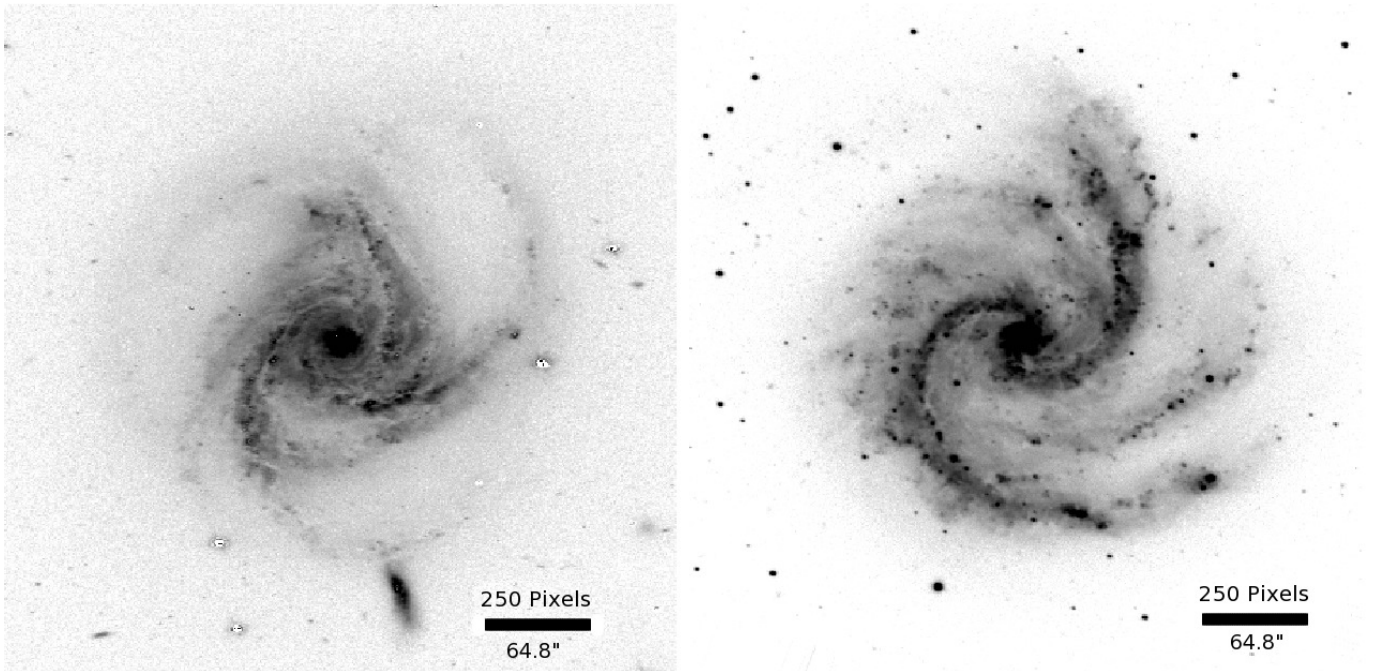

FIG. 10.— *Fig. 10a (left)* - Deprojected ($PA = 160°$ & $\alpha = 53.84°$) B-band (inverted color) image of NGC 5054. *Fig. 10b (right)* - Deprojected ($PA = 20°$ & $\alpha = 28.36°$) B-band (inverted color) image of NGC 5247.
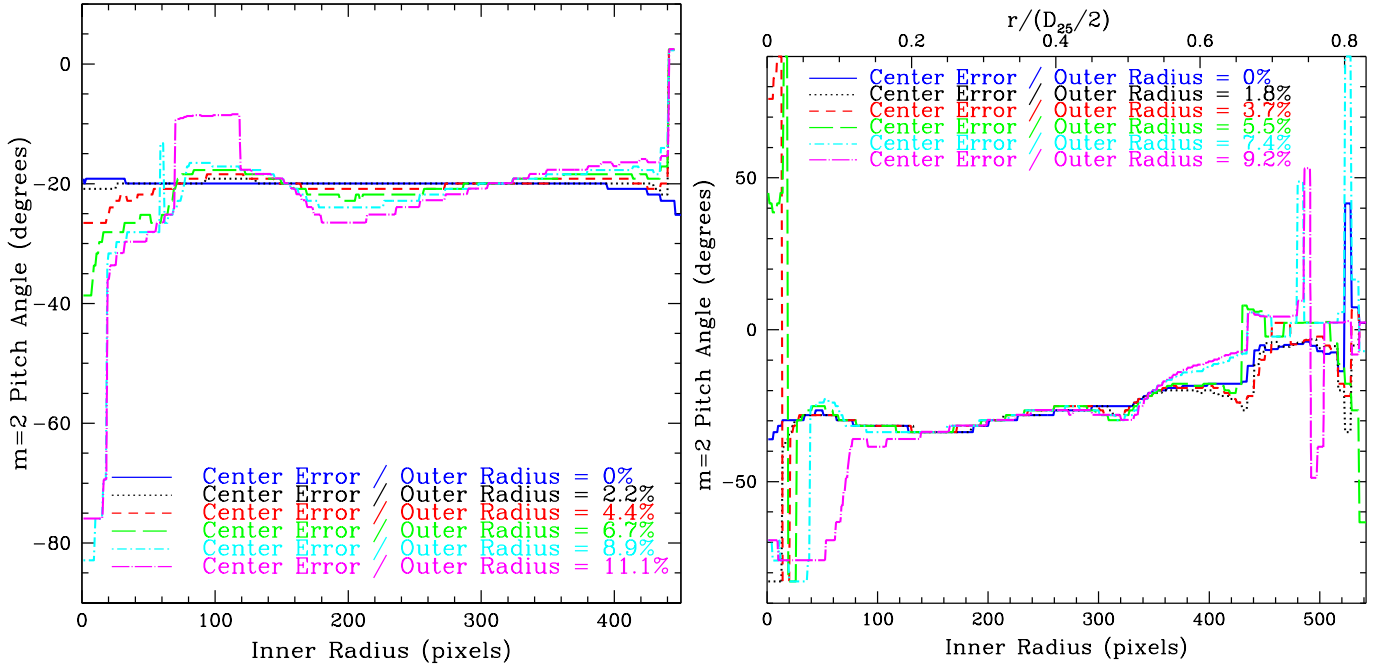
FIG. 11.— Center error tests on pitch angle for a synthetic two-armed logarithmic spiral (left) and a real two-armed galaxy (right). Errors of 10, 20, 30, 40, and 50 pixels from the previously determined center are used for both. *Fig. 11a (left)* - Pitch angle results for different errors in center determination for the synthetic two-armed spiral in Fig. 5b. As the error increases, the stable region gradually decreases, yet the approximate mean pitch angle remains about the same. *Fig. 11b (right)* - Real two-armed galaxy center test using a B-band image of NGC 5247 (see Fig. 10b) after deprojection ($PA = 38.71°$ & $\alpha = 25.18°$) was performed. The same case is true for the real galaxy image; the mean pitch angle remains constant despite a decreasing stable region with increasing error.
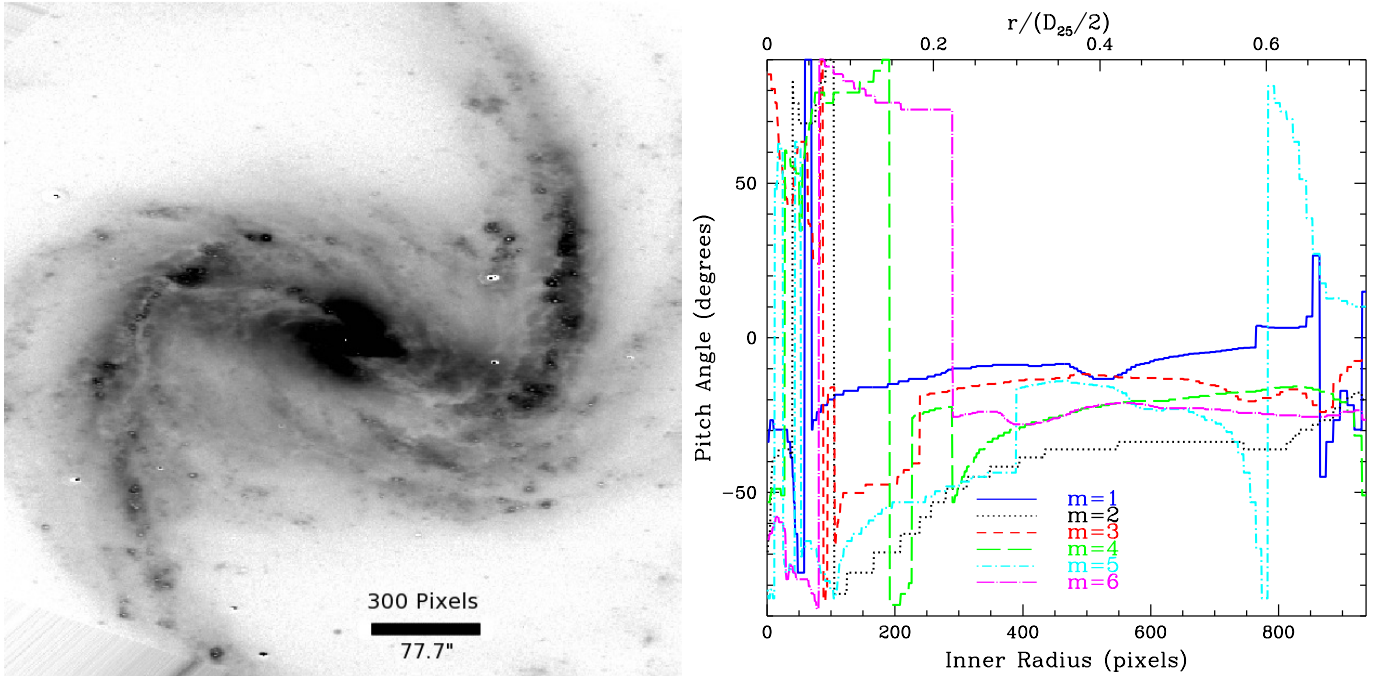
FIG. 12.— *Fig. 12a (left)* - Star-subtracted and deprojected B-band (inverted color) image of NGC 1365: $PA = 32°$ and $\alpha = 56.63°$. *Fig. 12b (right)* - Pitch angle as a function of inner radius for NGC 1365. A stable mean pitch angle of $-34.81°$ is determined for the $m = 2$ harmonic mode from a minimum inner radius of 451 pixels ($117''$) to a maximum inner radius of 812 pixels ($210''$), with an outer radius of 938 pixels ($243''$). This stretch of 361 pixels ($93.5''$) occupies 38% of the galactic disc. Equation 7 yields $E_\phi = 2.80°$ with $\lambda = 377$ pixels ($97.6''$), $\beta = 462$ pixels ($120''$), $\sigma = 1.17°$, and $\epsilon_2 = 2.40°$. The final determination of pitch angle is therefore $-34.81° \pm 2.80°$. This galaxy demonstrates a large bar, approximately 34% of its outer radius. The absolute value of the pitch angle can be seen to gradually decrease from $\phi = -82.87°$ at an inner radius of 105 pixels ($27.2''$) until $\phi = -36.03°$ at an inner radius of 435 pixels ($113''$), signaling the end of the bar.

TABLE 1
Pitch Angle/Wavelength Comparison

Galaxy Name	Morphology	α (deg.)	B-Band		I-Band	
			m	ϕ (deg.)	m	ϕ (deg.)
ESO 121-026	SB(rs)bc	50.95	2	10.06 ± 1.30	3	11.24 ± 3.05
ESO 582-012	SAB(rs)c	50.21	2	21.45 ± 2.32	2	23.54 ± 3.54
IC 2522	SB(s)c pec	44.77	3	-26.73 ± 4.69	5	-31.70 ± 5.15
IC 2537	SAB(rs)c	49.46	4	27.37 ± 3.84	4	34.11 ± 2.51
IC 3253	SA(s)c:	67.05	4	-17.53 ± 0.93	4	-13.50 ± 3.03
IC 4538	SAB(s)c:	39.65	4	-17.98 ± 2.61	3	-18.49 ± 5.20
IC 4831[a]	(R')SA(s)ab	77.47	2	-22.93 ± 2.41	2	-16.07 ± 1.46
NGC 150	SB(rs)b:	60.00	2	14.29 ± 4.26	1	23.15 ± 7.21
NGC 157	SAB(rs)bc	50.21	3	8.66 ± 0.89	3	9.32 ± 1.02
NGC 289	SB(rs)bc	44.77	5	19.71 ± 1.95	3	12.29 ± 1.36
NGC 578	SAB(rs)c	50.95	3	16.51 ± 1.88	2	24.24 ± 20.11
NGC 613	SB(rs)bc	40.54	3	21.57 ± 1.77	3	21.50 ± 2.06
NGC 908	SA(s)c	64.53	3	15.26 ± 2.61	2	32.12 ± 5.01
NGC 1187	SB(r)c	41.41	4	-21.96 ± 3.61	4	-21.55 ± 2.54
NGC 1232	SAB(rs)c	28.36	3	-25.71 ± 5.43	6	-31.51 ± 6.03
NGC 1292	SA(s)c	64.53	3	-15.89 ± 2.30	3	-16.34 ± 5.75
NGC 1337[a]	SA(s)cd	77.41	2	-16.53 ± 2.40	3	-19.58 ± 2.45
NGC 1353	SB(rs)b:	65.80	4	13.68 ± 2.31	4	13.21 ± 1.65
NGC 1365	SB(s)b	56.63	2	-34.81 ± 2.80	2	-35.94 ± 4.31
NGC 1559	SB(s)cd	55.25	2	-26.61 ± 9.69	2	-23.87 ± 2.87
NGC 1566	SAB(s)bc	36.87	2	-17.81 ± 3.67	2	-35.73 ± 5.10
NGC 1792	SA(rs)bc	60.00	3	-20.86 ± 3.79	3	-20.45 ± 3.20
NGC 1964	SAB(s)b	67.67	2	-12.86 ± 3.49	2	-7.85 ± 14.61
NGC 2082	SB(r)b	19.95	3	23.05 ± 7.90	3	16.91 ± 3.31
NGC 2090	SA(rs)c	60.00	4	4.91 ± 0.56	4	5.19 ± 0.60
NGC 2280	SA(s)cd	60.66	4	21.47 ± 2.87	2	13.98 ± 2.02
NGC 2835	SB(rs)c	47.93	3	-23.97 ± 2.22	3	-27.17 ± 2.68
NGC 2935	(R')SAB(s)b	38.74	2	-15.24 ± 4.72	2	-13.82 ± 5.32
NGC 3052	SAB(r)c:	49.46	3	-18.45 ± 1.59	2	-21.41 ± 3.46
NGC 3054	SAB(r)b	52.41	3	12.80 ± 1.77	3	10.56 ± 1.55
NGC 3223	SA(s)b	52.41	4	-10.92 ± 2.17	6	-27.79 ± 4.79
NGC 3261	SB(rs)b	40.54	6	15.38 ± 0.71	6	15.09 ± 0.78
NGC 3318	SAB(rs)b	57.32	3	35.58 ± 5.53	3	17.85 ± 4.89
NGC 3450	SB(r)b	28.36	6	-13.55 ± 0.31	2	-18.57 ± 5.48
NGC 3513	SB(rs)c	37.81	1	5.84 ± 1.46	1	6.26 ± 1.57
NGC 3887	SB(r)bc	40.54	4	-29.16 ± 4.82	4	-23.40 ± 4.08
NGC 4027	SB(s)dm	41.41	1	-12.06 ± 5.47	1	-10.58 ± 3.01
NGC 4030	SA(s)bc	44.77	3	23.48 ± 5.76	3	22.60 ± 6.52
NGC 4050	SB(r)ab	47.16	1	-6.32 ± 1.90	1	-6.85 ± 1.63
NGC 4930	SB(rs)b	34.92	3	30.29 ± 3.45	6	38.86 ± 2.24
NGC 4939	SA(s)bc	59.34	6	11.48 ± 1.71	6	13.95 ± 2.41
NGC 4995	SAB(rs)b	50.21	2	13.00 ± 2.88	6	9.27 ± 0.32
NGC 5054	SA(s)bc	53.84	3	-25.57 ± 3.72	3	-55.33 ± 9.07
NGC 5247	SA(s)bc	25.18	2	-31.94 ± 5.75	2	-36.16 ± 9.25
NGC 5483	SA(s)c	23.07	2	-22.98 ± 4.52	2	-22.31 ± 8.12
NGC 5967	SAB(rs)c:	53.84	3	18.26 ± 2.05	3	25.42 ± 3.60
NGC 6215	SA(s)c	30.68	4	-27.43 ± 5.85	4	-26.34 ± 5.95
NGC 6221	SB(s)c	44.77	6	-27.18 ± 2.14	6	-27.41 ± 3.19
NGC 6300	SB(rs)b	47.93	4	-16.58 ± 1.52	4	-16.61 ± 6.19

Note. — Col. (1) galaxy name; col. (2) morphological type from the RC3 (de Vaucouleurs et al. 1991); col. (3) inclination angle; col. (4) B-band dominant harmonic mode; col. (5) B-band pitch angle; col. (6) I-band dominant harmonic mode; and col. (7) I-band pitch angle.

[a] Not in Seigar et al. (2006) or plotted in Figure 13.

an outer radius interior to disrupted outer regions, we can confine our measurements to only the stable portions of M51a (see Figure 14c) and other similar galaxies.

4.3.3. Flocculence

Concerning the measurement of pitch angle of different types of spiral galaxies, flocculent spirals provide perhaps the biggest challenge. From our experience with flocculent galaxies, we find that our code most often finds them to have high-valued harmonic modes. Their characteristics can range from fragmented arms at best to chaos at worst. Elmegreen & Elmegreen (1987) defined a sys-

tem of arm classes and descriptions to categorize spirals into categories with varying degrees of flocculence. They defined 12 arm classes (classes 10 and 11 are no longer in use) with 12 having the most orderly spiral structure and 1 the least. Galaxies with arm classes 1-4 are considered flocculent, and those with arm classes 5-12 are grand design.

We have subsequently ascertained the arm classes (based on blue images from the Palomar Observatory Sky Survey) given by Elmegreen & Elmegreen (1987) for the galaxies we have measured for this paper and listed all available arm classes in Table 2. We have also cre-
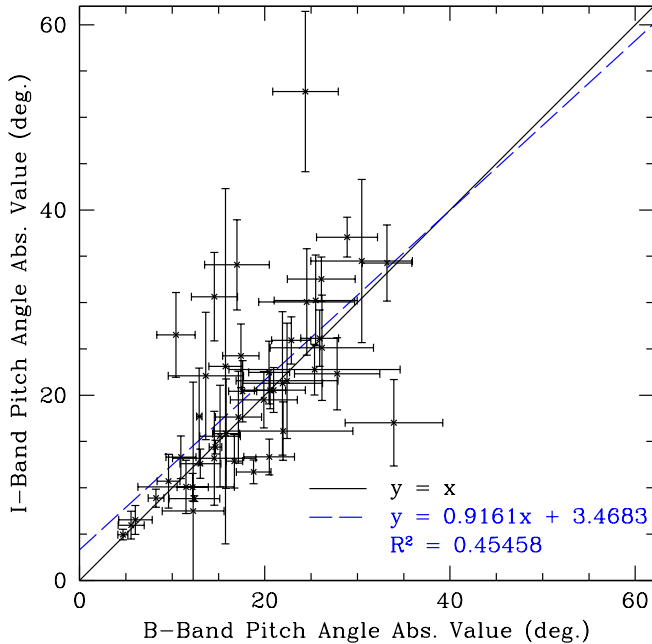
FIG. 13.— Pitch angles for 47 spiral galaxies in both blue (B) and infrared (I) wavebands. The solid black line represents a 1:1 ratio. The dashed blue line is a best-fit line, which is consistent with a 1:1 ratio within errors.

ated two plots (see Figure 15) of pitch angle absolute value vs. arm class (see Figure 15a) and pitch angle error vs. arm class (see Figure 15a) in order to investigate possible dependencies on arm classes. No clear relationship can be found from either plot, thus measurement of flocculent spirals do not appear to be inherently less precise than grand design spirals. However, our method of measuring pitch angle is very much dependent on the visual inspection conducted by the user. When initially inspecting images of possible candidate spiral galaxies for subsequent pitch angle measurement, it is more natural to be drawn to grand design spirals. This selection bias can be seen in selection of our sample for this paper without prior knowledge of their arm classes. Of the 48 galaxies listed in Table 2, only 8 galaxies are classified as being flocculent, with the remaining galaxies all classified as being grand design spirals. It is our practice to only attempt pitch angle measurement on galaxies that display convincing evidence of definable spiral structure from image inspection. From our study of the CGS sample thus far, we have been able to convincingly measure pitch angles for 62% of the spiral galaxies we have examined; 17% of the galaxies were rejected due to their high angle of inclination and the remaining 21% were omitted due to a lack of discernible spiral structure (of this 21%, among those with arm classifications from Elmegreen & Elmegreen (1987), 60% were classified as flocculent).

5. IMAGE ANALYSIS

The sign of the pitch angle and the number of harmonic modes are very important for correct image analysis. As the pitch angle is calculated over all possible values of inner radii for a galaxy, it is not uncommon for pitch angle to vary drastically in different harmonic modes. Different harmonic modes will have different signs of pitch angle

and even across one harmonic mode, sign changes may occur. The most apparent feature to the human eye, for discernable spiral arms, is the chirality of the spiral arms. As a result, harmonic modes that favor opposing chirality can immediately be ruled out after a quick visual inspection of the image.

For galaxies with visually distinctive spiral arms, it is simple enough to count the number of spiral arms by eye and adopt that number of arms as the correct harmonic mode. However, in flocculent galaxies or galaxies with galactic arm spurs, it maybe necessary to adopt other methods in selecting the correct harmonic mode. Typically, the harmonic mode with the largest region of stable pitch angle across inner radii is the most valuable for our purposes. Nonetheless, other aspects of the code can lend a hand in identifying the dominant harmonic mode. The easiest method is by plotting the amplitude of p_{max} as a function of inner radius. This will help identify the harmonic mode with the strongest amplitude over the largest radial range of the galaxy. For NGC 5054 (see Figure 16b), the $m = 3$ harmonic mode is dominant (Block et al. 1999) over the outer 84.8% of the galaxy's radius. In many cases, several harmonic modes agree reasonably well as to the pitch angle. In addition, producing an image of the Inverse FFT of a harmonic mode can help visually identify the "correct" harmonic mode (see §5.2).

5.1. Symmetrical Component Significance

It is a likely possibility that all of the arms of a spiral galaxy, especially galaxies with multiple arms, might not be perfectly symmetric. This could be the result of tidal disruption, galaxy harassment, etc. Whatever the reason, slight imperfections should be handled by the robustness of the FFT. A common trend among galaxies we have analyzed is that some galaxies exhibit spiral arms which gradually tighten, or decrease in absolute value of pitch angle, toward the outer regions of the galaxy (see Figures 10a and 17a). For galaxies with drastically asymmetric spiral arms or arms which demonstrate variable pitch angle, we use the method of Elmegreen et al. (1992) to isolate the symmetrical component of a galaxy (see Figure 18) and then we perform a pitch angle determination on the symmetrical component (see Figures 17b and 19b). Symmetric parts of galaxies are illustrated by making images from successive rotations and subtractions. The procedure of Elmegreen et al. (1992) is

$$S_m(r,\theta) = (m-1)F(r,\theta) - \sum_{j=1}^{m-1}[F(r,\theta) - F(r,\theta - \frac{2j\pi}{m})]_T$$

(8)

where for $m \geq 2$, S_m is the image displaying the m-fold symmetric part of a galaxy made from the original image F, and the subscript T stands for truncation, meaning that pixels with negative intensities are set to zero. For the case of a two-armed spiral galaxy, the S_2 image consists of all bright features in the original image that have equally bright features diametrically across the galaxy. This procedure highlights symmetric emission, such as spiral arm spurs, star formation regions, etc., but it introduces spurious absorption features. For example, if there is a dust lane in only one arm, then only the bright part of that arm will appear in both arms of the S_2 im-
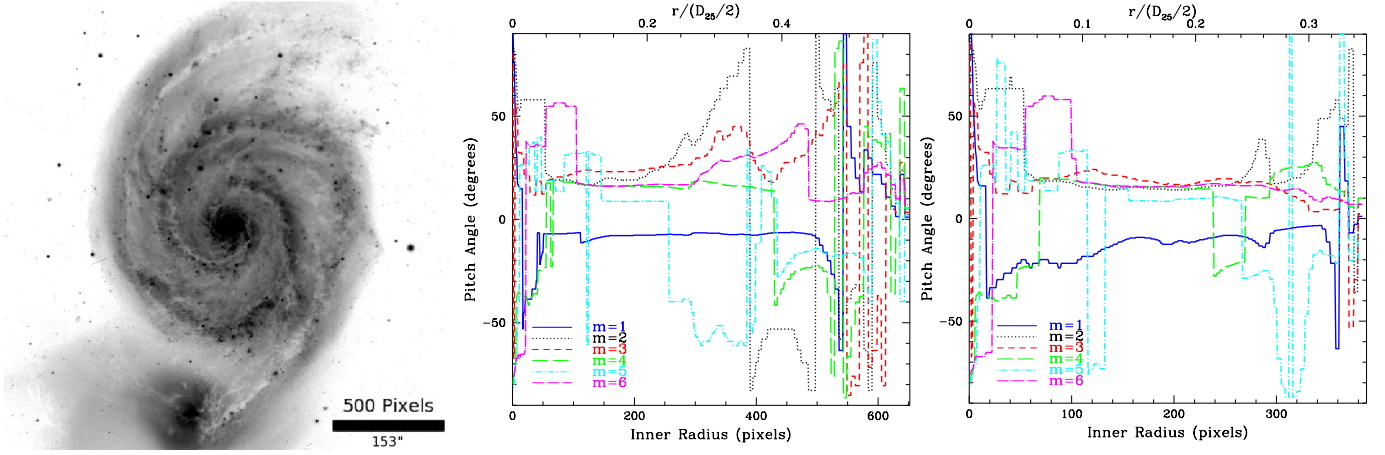
FIG. 14.— *Fig. 14a (left)* - Deprojected ($PA = -154.1°$ & $\alpha = 19.09°$) B-band (inverted color) image of M51 (M51a and its dwarf companion galaxy M51b) acquired from NED (imaging from KPNO 2.1 m CFIM with a pixel scale of $0.305''$ pixel^{-1}). *Fig. 14b (middle)* - A stable mean pitch angle of $19.13°$ is determined for the $m = 2$ harmonic mode from a minimum inner radius of 54 pixels ($16.5''$) to a maximum inner radius of 229 pixels ($69.8''$), with an outer radius of 653 pixels ($199''$). This stretch of 175 pixels ($53.4''$) occupies 27% of the galactic disc. Equation 7 yields $E_\phi = 4.76°$ with $\lambda = 175$ pixels ($53.4''$), $\beta = 534$ pixels ($163''$), $\sigma = 1.54°$, and $\epsilon_2 = 0.78°$. The final determination of pitch angle is therefore $19.13° \pm 4.76°$. Due to the interaction with its companion galaxy, M51a shows a significant departure from a constant pitch angle in the outer regions of the galaxy. This is seen in Fig. 14a and at the noticeable sign change in this plot at an inner radius of 389 pixels ($119''$). *Fig. 14c (right)* - A stable mean pitch angle of $16.26°$ is determined for the $m = 2$ harmonic mode from a minimum inner radius of 54 pixels ($16.5''$) to a maximum inner radius of 276 pixels ($84.2''$), with an outer radius of 389 pixels ($119''$). This stretch of 222 pixels ($67.7''$) occupies 57% of the measurement annulus. Equation 7 yields $E_\phi = 3.20°$ with $\lambda = 222$ pixels ($67.7''$), $\beta = 296$ pixels ($90.3''$), $\sigma = 2.36°$, and $\epsilon_2 = 0.57°$. The final determination of pitch angle is therefore $16.26° \pm 3.20°$. This alternate pitch angle measurement isolates the inner portion of the galaxy out to the clear break from constant pitch angle seen in Fig.14b. As a result, the unstable outer portion of the galaxy has been ignored and a more accurate pitch angle has been determined for the purer inner structure of this interacting galaxy.
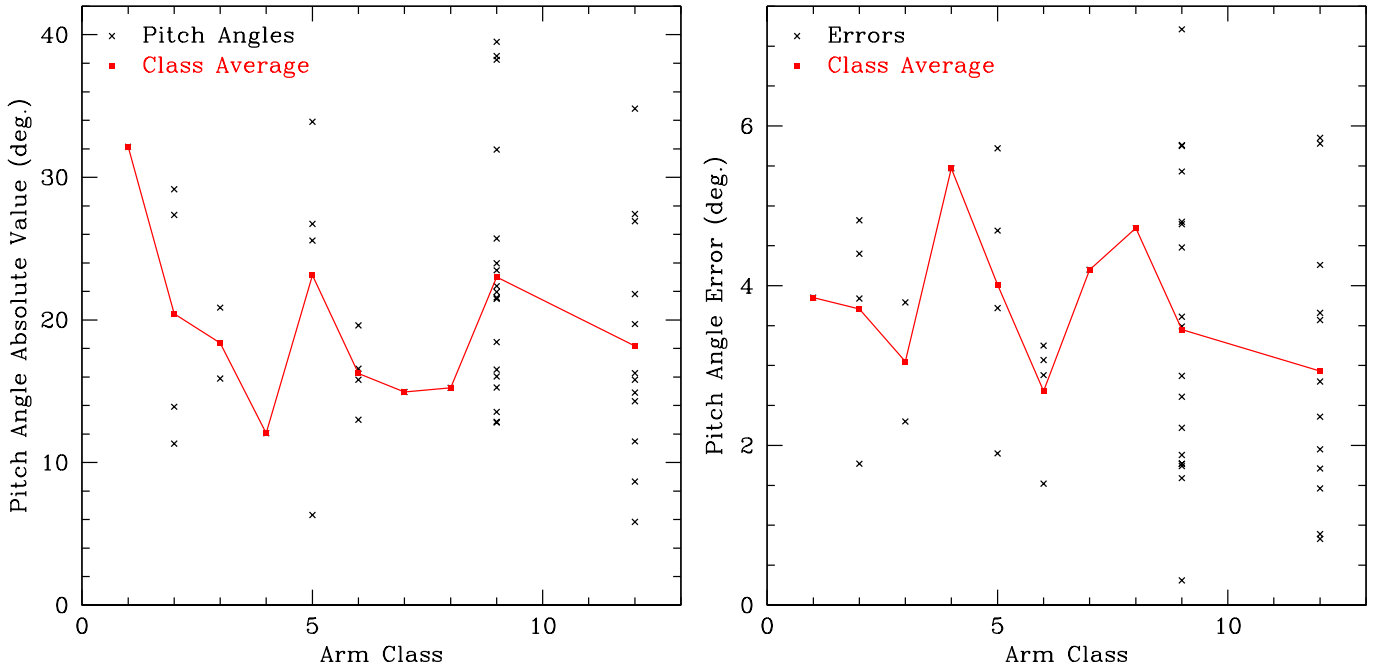
FIG. 15.— Pitch angles (left) and their associated errors (right) sorted into their respective arm classes (classes 10 and 11 are no longer in use). *Fig. 15a (left)* - Pitch angles (black crosses) arranged into their arm classes with binned averages (red squares connected by red line segments). No clear trend is recognizable between pitch angle and arm class. *Fig. 15b (right)* - Pitch angle errors (black crosses) arranged into their arm classes with binned averages (red squares connected by red line segments). No clear trend is recognizable between pitch angle errors and arm class.

TABLE 2
PITCH ANGLES AND ARM CLASSES

Galaxy Name	Morphology	m	ϕ (deg.)	Band	Source	Arm Class
IC 2522	SB(rs)bc	3	-26.73 ± 4.69	B	1	5
IC 2537	SAB(rs)c	4	27.37 ± 3.84	B	1	2
M51a	SA(s)bc pec	2	16.26 ± 2.36	B	3	12
NGC 45	SA(s)dm	3	-32.13 ± 3.85	B	1	1
NGC 150	SB(rs)b:	2	14.29 ± 4.26	B	1	12
NGC 157	SAB(rs)bc	3	8.66 ± 0.89	B	1	12
NGC 210	SAB(s)b	2	-15.81 ± 3.25	B	1	6
NGC 289	SB(rs)bc	5	19.71 ± 1.95	B	1	12
NGC 578	SAB(rs)c	3	16.51 ± 1.88	B	1	9
NGC 598	SA(s)cd	2	-33.90 ± 5.72	6450 Å[a]	2	5
NGC 613	SB(rs)bc	3	21.57 ± 1.77	B	1	9
NGC 895	SA(s)cd	2	-38.50 ± 4.77	I	1	9
NGC 908	SA(s)c	3	15.26 ± 2.61	B	1	9
NGC 1042	SAB(rs)cd	4	39.50 ± 4.48	R	1	9
NGC 1097[b]	SB(s)b	2	15.80 ± 3.62	I	1	12
NGC 1187	SB(r)c	4	-21.96 ± 3.61	B	1	9
NGC 1232	SAB(rs)c	3	-25.71 ± 5.43	B	1	9
NGC 1292	SA(s)c	3	-15.89 ± 2.30	B	1	3
NGC 1300	SB(rs)bc	2	-12.71 ± 1.99	B	1	12
NGC 1365	SB(s)b	2	-34.81 ± 2.80	B	1	12
NGC 1398	(R$'$)SB(r)ab	4	19.61 ± 3.07	V	1	6
NGC 1566	SAB(s)bc	2	-17.81 ± 3.67	B	1	12
NGC 1792	SA(rs)bc	3	-20.86 ± 3.79	B	1	3
NGC 1964	SAB(s)b	2	-12.86 ± 3.49	B	1	9
NGC 2280	SA(s)cd	4	21.47 ± 2.87	B	1	9
NGC 2442	SAB(s)bc pec	2	14.95 ± 4.20	V	1	7
NGC 2835	SB(rs)c	3	-23.97 ± 2.22	B	1	9
NGC 2935	(R$'$)SAB(s)b	2	-15.24 ± 4.72	B	1	8
NGC 3052	SAB(r)c:	3	-18.45 ± 1.59	B	1	9
NGC 3054	SAB(r)b	3	12.80 ± 1.77	B	1	9
NGC 3450	SB(r)b	6	-13.55 ± 0.31	B	1	9
NGC 3513	SB(rs)c	1	5.84 ± 1.46	B	1	12
NGC 3783	(R$'$)SB(r)ab	2	10.71 ± 0.64	B	1	9
NGC 3887	SB(r)bc	4	-29.16 ± 4.82	B	1	2
NGC 3938	SA(s)c	4	-22.37 ± 7.21	B	3	9
NGC 4027	SB(s)dm	1	-12.06 ± 5.47	B	1	4
NGC 4030	SA(s)bc	3	23.48 ± 5.76	B	1	9
NGC 4050	SB(r)ab	1	-6.32 ± 1.90	B	1	5
NGC 4321	SAB(s)bc	5	21.81 ± 3.57	R	3	12
NGC 4939	SA(s)bc	6	11.48 ± 1.71	B	1	12
NGC 4995	SAB(rs)b	2	13.00 ± 2.88	B	1	6
NGC 5054	SA(s)bc	3	-25.57 ± 3.72	B	1	5
NGC 5085	SA(s)c	2	-11.32 ± 1.77	4680 Å[c]	4	2
NGC 5236	SAB(s)c	6	-16.04 ± 1.74	B	1	9
NGC 5247	SA(s)bc	2	-31.94 ± 5.75	B	1	9
NGC 5861	SAB(rs)c	2	-14.91 ± 0.83	V	1	12
NGC 6215	SA(s)c	4	-27.43 ± 5.85	B	1	12
NGC 6300	SB(rs)b	4	-16.58 ± 1.52	B	1	6
NGC 7793	SA(s)d	2	13.91 ± 4.40	B	1	2

NOTE. — Col. (1) galaxy name; col. (2) morphological type from the RC3 (de Vaucouleurs et al. 1991); col. (3) dominant harmonic mode; col. (4) pitch angle; col. (5) waveband/wavelength; col. (6) telescope/survey imaging source; and col. (7) arm class from Elmegreen & Elmegreen (1987). Source (1) CGS; source (2) Palomar 48 inch Schmidt; source (3) KPNO 2.1 m CFIM; and source (4) UK 48 inch Schmidt.

[a] 103aE emulsion.
[b] In addition to spiral arms in the disc of the galaxy, NGC 1097 displays rare $m = 2$ nuclear spiral arms in the bulge. These arms display an opposite chirality to the disc arms with $\phi = -30.60° \pm 2.68°$.
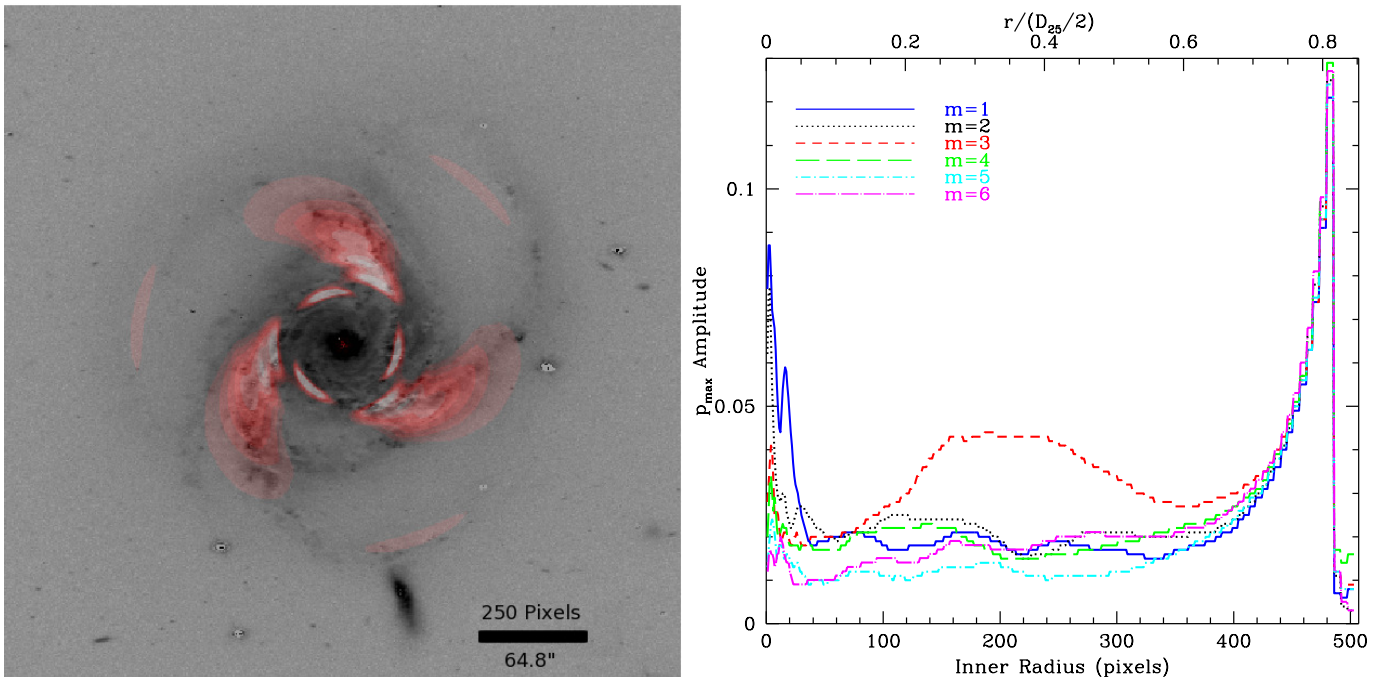[c] IIIaJ emulsion.

FIG. 16.— *Fig. 16a (left)* - Star-subtracted and deprojected ($PA = 160°$ & $\alpha = 53.84°$) B-band (inverted color) image of NGC 5054 (see Fig. 10a), overlaid with the contours of the Inverse 2-D FFT for the $m = 3$ harmonic mode (in red) conducted with an inner radius of 160 pixels ($41.4''$) and an outer radius of 508 pixels ($132''$). The contours are the real part of the complex spatial function of Equation 9 with $m = 3$. The contours illustrate the different levels of amplitude for the $m = 3$ harmonic mode. The Inverse 2-D FFT displays a single value pitch angle of $-40.60°$ (as shown in Fig. 1b). However, the pitch angle can be seen to tighten (decrease) as the inner radius increases. *Fig. 16b (right)* - Plot of the amplitude of p_{max} as a function of inner radius for NGC 5054, indicating the $m = 3$ component as the dominant harmonic mode for the galaxy. The $m = 3$ harmonic mode is dominant from an inner radius of 77 to 456 pixels ($19.9''$ to $118''$), constituting about 75% of the galaxy's radius.

age; this gives the false impression that there is a dust lane in the other arm also. This method appears to decrease our error estimates when performed. For galaxies with apparent initial symmetry, the mean pitch angle is not changed significantly; e.g., NGC 5247 (see Figure 19), the percent difference in mean pitch angle is 10.48% with essentially the same error. This tool seems most useful for galaxies that display variable pitch angle (see Figure 17). Error estimates can be reduced drastically for these cases; e.g., NGC 5054, for which the percent difference in mean pitch angle is 4.19% with a 72.03% decrease in error. Moreover, this process can act as an effective substitute for star subtraction.

5.2. *Two-Dimensional Inverse Fast Fourier Transform*

One of the most powerful tools provided by *2DFFT* is the ability to run an Inverse FFT. After having deprojected the images and identified the dominant harmonic modes, we can calculate the inverse of the transforms according to Seigar et al. (2005). The inverse transform can be written as

$$S(u, \theta) = \sum_m S_m(u)e^{im\theta} \qquad (9)$$

where

$$S_m(u) = \frac{D}{e^{2u}4\pi^2} \int_{p_-}^{p_+} G_m(p)A(p,m)e^{ipu}dp. \qquad (10)$$

$G_m(p)$ is a high-frequency filter used by Puerari & Dottori (1992). For the logarithmic spiral governed by Equa-

tion 4, it has the form

$$G_m(p) = e^{-\frac{1}{2}(\frac{p-p_{max}}{25})^2}. \qquad (11)$$

This filter is also used to smooth the $A(p,m)$ spectra at the interval ends ($p_- = -50$ and $p_+ = 50$ with $dp = 0.25$) (Puerari & Dottori 1992). Equation 9 is designed as such, to allow the user to create an inverse transform for a selected number of harmonic components. For example, the inverse transform can be calculated for one component, e.g., $m = 2$, or any number of components can be combined to yield a composite result, e.g., $m = 2, 3,$ & 4.

Once an Inverse FFT is created, it can be directly compared to the deprojected image of the galaxy, allowing us to effectively observe what the code is seeing. Figure 16a and Figure 20 show images of spiral galaxies overlaid with contours representing the results of Inverse FFTs of the same galaxy. The contours are the real part of the complex spatial function of Equation 9. The use of these images to analyze a galaxy can lead to more confident determination of pitch angle.

6. DISCUSSION AND FUTURE WORK

Our modified version of *2DFFT* is a powerful tool for accurately measuring galactic spiral arm pitch angle. Our software, combined with careful image and data inspection, comparative pitch angle selection, and a self-regulating error determination allows for reliable pitch angle measurements. We hope that quantitative determinations of spiral arm pitch angle will aid in galaxy classification, in the indirect study of central black hole masses and more generally in our understanding of galac-
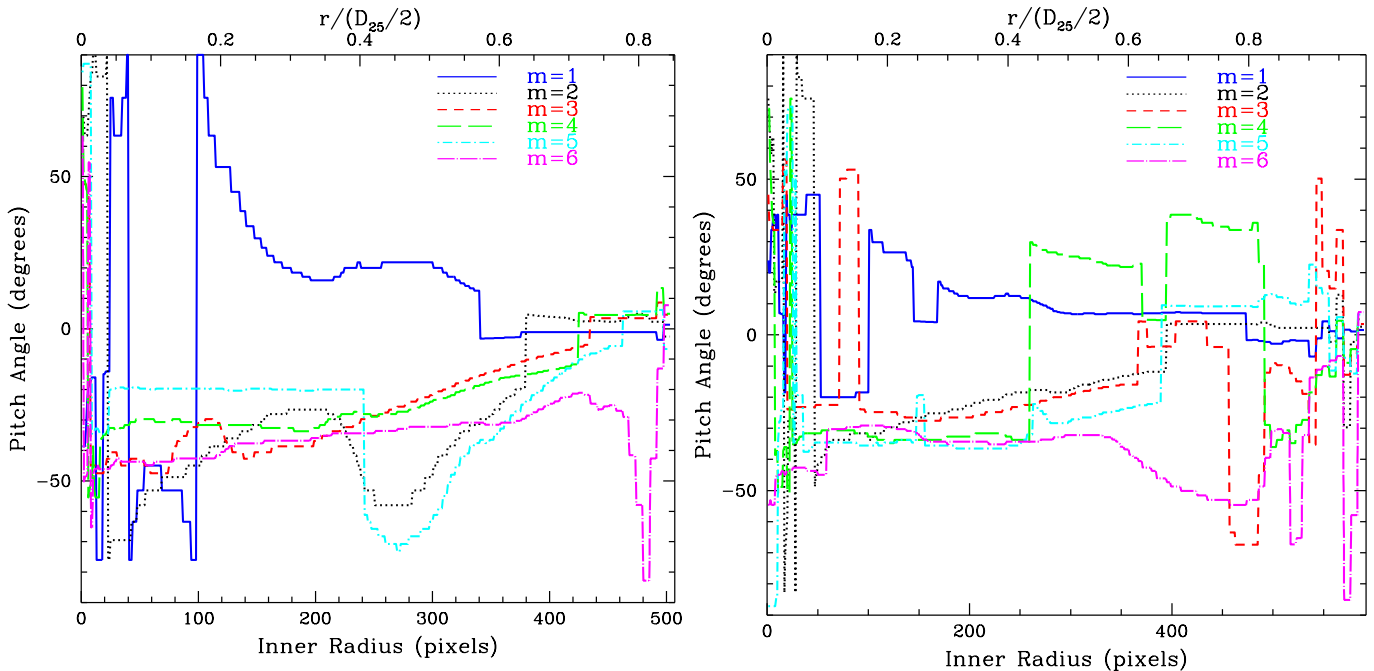
FIG. 17.— *Fig. 17a (left)* - B-band pitch angle as a function of inner radius for NGC 5054, after star subtraction and deprojection ($PA = 160°$ & $\alpha = 53.84°$) were performed (see Fig. 10a). A stable mean pitch angle is difficult to define since the pitch angle is seen to continually decrease from an inner radius of about 200 to one of about 425. A rough mean pitch angle of $-24.52°$ (a significant departure from the single value, non-iterative measurement of $-40.60°$, see Fig. 1b) is determined for the $m = 3$ harmonic mode from a minimum inner radius of 123 pixels ($31.9''$) to a maximum inner radius of 434 pixels ($112''$), with an outer radius of 508 pixels ($132''$). This stretch of 311 pixels ($80.5''$) occupies 61% of the galactic disc. This measurement has a significant error due to the unstable pitch angle. Equation 7 yields $E_\phi = 12.84°$ with $\lambda = 311$ pixels ($80.5''$), $\beta = 334$ pixels ($86.5''$), $\sigma = 11.92°$, and $\epsilon_3 = 0.92°$. The final determination of pitch angle is therefore $-24.52° \pm 12.84°$. *Fig. 17b (right)* - For the pure symmetrical component of NGC 5054 (see Fig. 18a), the B-band pitch angle (same deprojection parameters as Fig. 17a) as a function of inner radius is far more stable. A stable mean pitch angle of $-25.57°$ is determined for the $m = 3$ harmonic mode from a minimum inner radius of 91 pixels ($23.6''$) to a maximum inner radius of 253 pixels ($65.5''$), with an outer radius of 593 pixels ($154''$). This stretch of 162 pixels ($42.0''$) occupies 27% of the galactic disc. Equation 7 yields $E_\phi = 3.72°$ with $\lambda = 162$ pixels ($42.0''$), $\beta = 443$ pixels ($115''$), $\sigma = 1.31°$, and $\epsilon_2 = 1.00°$. The final determination of pitch angle is therefore $-25.57° \pm 3.72°$, a percent difference of 4.19% in mean pitch angle with a 72.03% reduction in error from the original.

tic morphology and its evolution. One important advantage of this means of describing galaxies is its relative ease of acquisition, since only imaging data is required to measure it. Also, it provides us with great opportunity to test competing theories behind galactic spiral arm genesis (Martínez-García 2012).

6.1. *Comparison to Other Methods*

Our method adds one dimension to recently published FFT methods (e.g., Kendall et al. 2011). In doing so, we are able to effectively use more of the inherent information in the images. Alternatively, 1-D methods identify radial peaks in intensity azimuthally about the galactic center by use of radial search segments that ultimately do not utilize the full resolution of the image. Admittedly, our method comes at a higher price in terms of computing power to analyze the full resolution of an image, but with modern computational power, this computational expense is trivial and is easily handled by modern processors. Ultimately, users of both 1-D and 2-D FFT methods are still obliged to visually inspect images. As for flocculent galaxies, 1-D FFT methods are admittedly only equipped to handle grand design spirals. Our 2-D FFT, though it may occasionally encounter trouble with high degrees of flocculence, will perform adequately with flocculent galaxies and with the support of additional image analysis methods (see §5 and its subsec-

tions) and multi-wavelength imaging, it can confidently approach any galaxy with hints of spirality. Additionally, our pitch angle measurements are unique in that fact that we measure and quote pitch angles for multi-armed galaxies (dominant harmonic modes $m > 2$). Other researchers may have analyzed and discussed the influences from higher order harmonic modes, but in the end always publish pitch angles resulting from harmonic modes $m \leq 2$.

In order to compare the results of our method to other published methods, we have chosen a well-studied sample of galaxies whose pitch angles have been determined independently, using different techniques in the literature. For this sample, we have selected the results of Martínez-García (2012), Kendall et al. (2011), Ma (2001), Grosbol & Patsis (1998), and Kennicutt (1981) as references with which to compare our measurements (see Table 3). These five references provide a nice spread in measurement methods. Kennicutt (1981) used $H\alpha$ photographic plates and subsequent by-hand geometric measurements of nearby Sa-Sc galaxies to calculate average pitch angles determined from the two main arms in each galaxy[8];

[8] Savchenko & Reshetnikov (2011) remeasured pitch angles for 46 of the spiral galaxies measured by Kennicutt (1981) with two distinct methods: by-hand and 1-D FFT analysis. Results of both methods show good mutual agreement with the mean differences between measurements less than a few degrees in both cases.
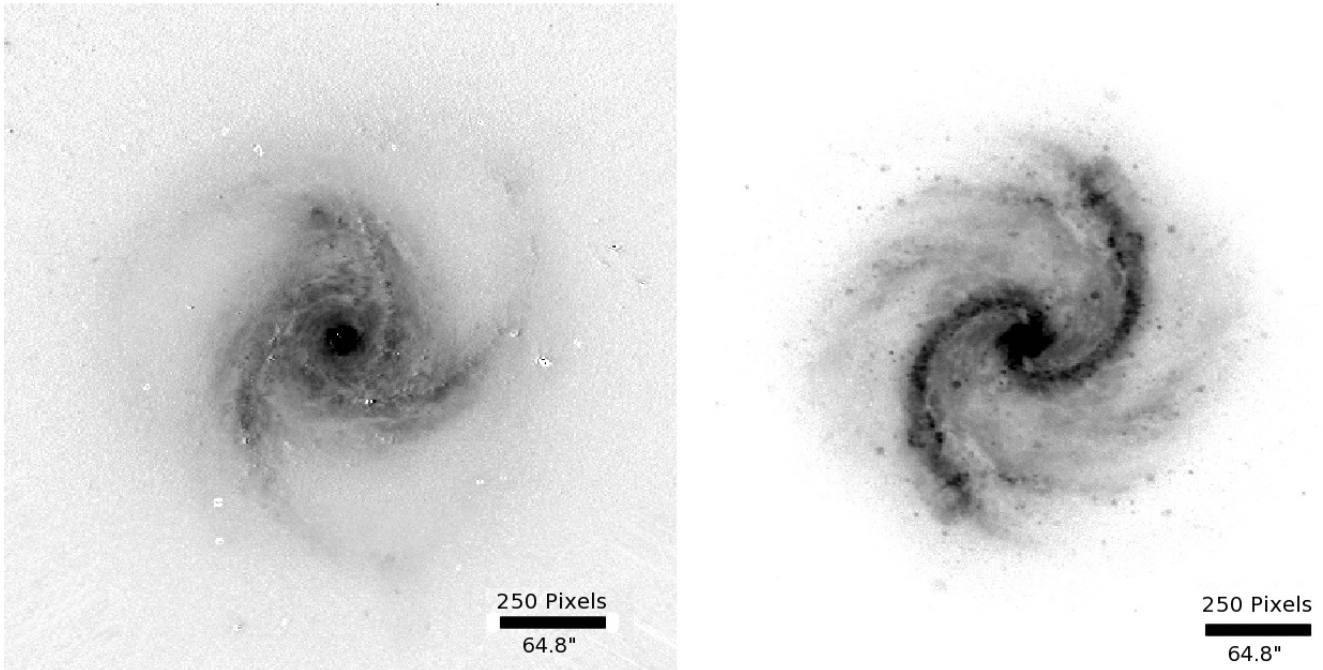
FIG. 18.— *Fig. 18a (left)* - $m = 3$ symmetrical component (inverted color and with the same deprojection parameters as Fig. 10a) of NGC 5054 (see Fig. 10a). *Fig. 18b (right)* - $m = 2$ symmetrical component (inverted color and with the same deprojection parameters as Fig. 10b) of NGC 5247 (see Fig. 10b).

Grosbol & Patsis (1998) utilized accurate surface photometry and derivation of axisymmetric components to calculate $m = 2$ pitch angles for five galaxies from the residuals of intensive image processing and Fourier components of the azimuthal intensity variations; Ma (2001) visually selected points along spiral arms in CCD images of galaxies and fit logarithmic spirals to the points; Kendall et al. (2011) employed 1-D FFT decomposition to calculate $m = 2$ pitch angles for a sample of grand design spiral galaxies; and Martínez-García (2012) used both a "slope method" and adopted a 2-D FFT algorithm similar to our own, but without our analysis of pitch angle as a function of inner radius.

Table 3 compares 38 of our pitch angle measurements against available measurements from five independent sources. The mean difference between the measurements for the same galaxies are as follows: $\Delta\phi_1 = -5.13° \pm 19.41°$ (the difference between our measured pitch angles and those of Martínez-García 2012) or $\Delta\phi_1 = -0.11° \pm 7.38°$ if the outlying measurement of NGC 4995 is disregarded, $\Delta\phi_2 = 1.73° \pm 3.58°$ (the same for Kendall et al. 2011), $\Delta\phi_3 = 0.66° \pm 9.97°$ (the same with the average arm measurement from Ma 2001), $\Delta\phi_4 = 2.93° \pm 1.71°$ (the same for Grosbol & Patsis 1998), and $\Delta\phi_5 = 5.15° \pm 8.66°$ (the same for Kennicutt 1981). These differences are comparable to the mean error in our measurements for this sample: $\phi_E = 3.34° \pm 1.94°$.

6.1.1. *NGC 7083*

For individual measurements, several differences can be explained by our selection of a different harmonic mode from that chosen by the other group. For example, our measurement of NGC 7083 differs from the measurement by Grosbol & Patsis (1998); $-19.44° \pm 3.21°$ and

$-15.0° \pm 1.0°$, respectively. This can be explained by our selection of the $m = 3$ harmonic mode and their selection of the $m = 2$ harmonic mode (see Figure 21). In short, we believe this is a three-armed galaxy, not two-armed, a finding supported by the strength of our code's $m = 3$ harmonic mode and by visual inspection. It is of note that we find our measurement of the $m = 4$ harmonic mode's pitch angle to be $-15.38° \pm 2.97°$ (see Figure 21c), which coincides with the measurement of Grosbol & Patsis (1998). However, our measurement of the $m = 2$ harmonic mode is not possible due to its chiral instability. Despite the nice agreement of pitch angle between our $m = 4$ pitch angle and their $m = 2$ pitch angle, we find strong indications that the dominant harmonic mode is $m = 3$ (see Figure 21b).

6.1.2. *NGC 4995*

NGC 4995 depicts a significant outlier from the pitch angle measurement of Martínez-García (2012); $78.3^{+5.4}_{-8.3}$ degrees compared to our measurement of $13.00° \pm 2.88°$. Their enormously high measured pitch angle is most sensibly unphysical, along with any measurement of $\phi \gtrsim 60°$.

6.1.3. *NGC 1365*

A big discrepancy can be seen in comparison of our measurement of NGC 1365, $-34.81° \pm 2.80°$, to the pitch angle absolute value measurements of Ma (2001), $13.8°$ & $17.8°$, and Kennicutt (1981), $18° \pm 3°$. We find strong indications both from our code (see Figure 12) and visually (see Figure 22) that the pitch angle beyond the large bar is on the high side. In order to visually compare the fit of two logarithmic spirals with different pitch angles, the scaling must be adjusted. According to Equation 1, the radius of a logarithmic spiral with a higher pitch angle will grow much more rapidly than a logarith-
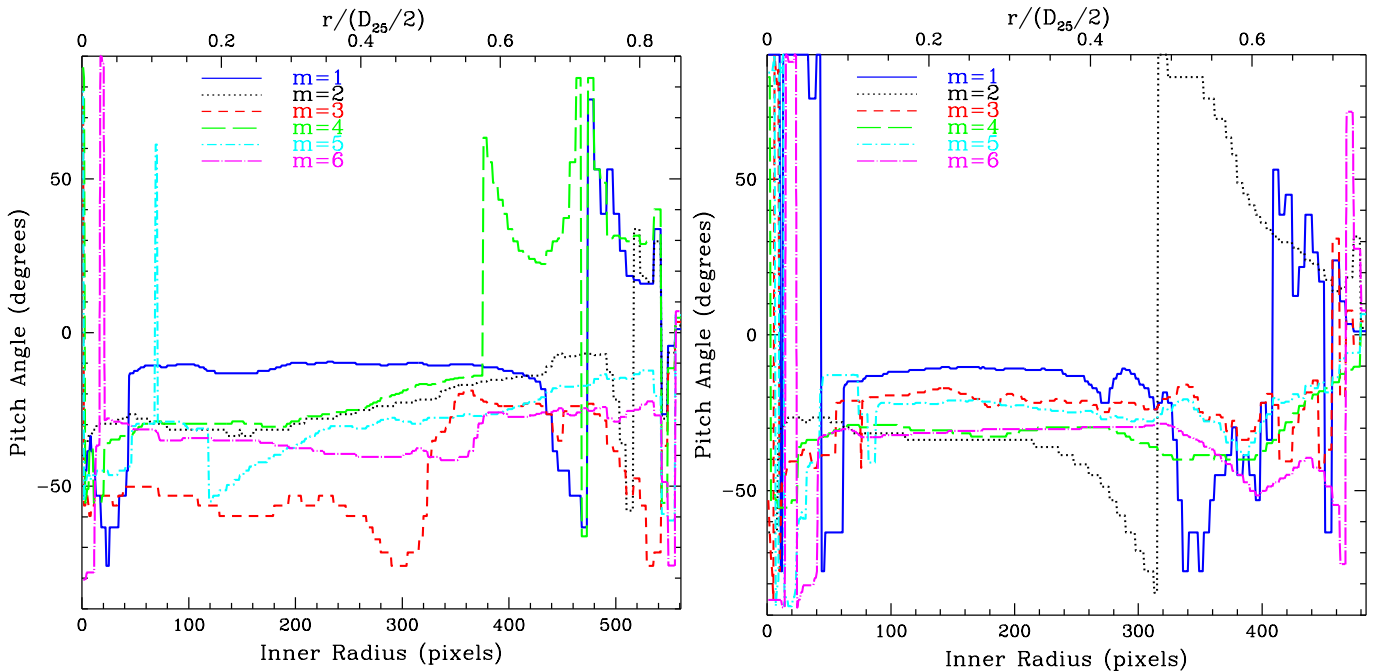
FIG. 19.— *Fig. 19a (left)* - B-band pitch angle as a function of inner radius for NGC 5247 after deprojection ($PA = 20°$ & $\alpha = 28.36°$) was performed (see Fig. 10b). A stable mean pitch angle of $-28.76°$ is determined for the $m = 2$ harmonic mode from a minimum inner radius of 1 pixel ($0.259''$) to a maximum inner radius of 331 pixels ($85.7''$), with an outer radius of 565 pixels ($146''$). This stretch of 330 pixels ($85.5''$) occupies 58% of the galactic disc. Equation 7 yields $E_\phi = 5.73°$ with $\lambda = 330$ pixels ($85.5''$), $\beta = 508$ pixels ($132''$), $\sigma = 3.56°$, and $\epsilon_2 = 1.70°$. The final determination of pitch angle is therefore $-28.76° \pm 5.73°$. *Fig. 19b (right)* - For the pure symmetrical component of NGC 5247 (see Fig. 18b), a stable mean B-band pitch angle (same deprojection parameters as Fig. 19a) of $-31.94°$ is determined for the $m = 2$ harmonic mode from a minimum inner radius of 9 pixels ($2.33''$) to a maximum inner radius of 235 pixels ($60.9''$), with an outer radius of 486 pixels ($126''$). This stretch of 226 pixels ($58.5''$) occupies 47% of the galactic disc. Equation 7 yields $E_\phi = 5.75°$ with $\lambda = 226$ pixels ($58.5''$), $\beta = 428$ pixels ($111''$), $\sigma = 2.83°$, and $\epsilon_2 = 2.06°$. The final determination of pitch angle is therefore $-31.94° \pm 5.75°$, a percent difference of 10.48% in mean pitch angle with essentially the same error as the original. As a characteristic example, NGC 5247 displays a similar pattern of agreement among even harmonic modes as the two-armed synthetic spiral with an added symmetrical bulge component (see Figure 5g).

mic spiral with a lower pitch angle. In order to allow the radius of the $\phi = 16.5°$ logarithmic spiral to grow at the same rate as the three higher pitch angle logarithmic spirals in Figure 22, we multiplied its resulting radius by a factor of 2.8. When optimally scaled, our high pitch angle measurement and their low pitch angle measurements can be brought into rough agreement. The difficulty in accurately measuring pitch angle increases as the amount of angular wrapping around a galaxy decreases, i.e., $\theta_{max} \simeq \frac{\pi}{2}$ for NGC 1365 whereas the spirals do not become significantly different until $\theta \gtrsim \frac{3\pi}{4}$ at the edge of Figure 22. Furthermore, NGC 1365 is a well-documented case of variable pitch angle (Ringermacher & Mead 2009) with high pitch angle near the arm-bar junction and low pitch angle in the outermost regions of the galaxy. Our code correctly identifies this high pitch angle near the arm-bar junction and provides us with our desired innermost stable pitch angle of the galaxy (see §4.3.2).

6.1.4. *NGC 3513*

NGC 3513 demonstrates a case where Ma (2001) measures dramatically different pitch angles between two arms ($18.2°$ & $8.1°$). Our measurement of $5.84° \pm 1.46°$ for the $m = 1$ component is in near agreement with the smaller of Ma's two measurements. From inspection of the image of NGC 3513, it appears to have one arm with near-constant pitch angle and another, more ambiguous

arm, with a clear kink in it. The forced inclusion of the non-logarithmic arm might also be responsible for making Martínez-García's 2-D FFT measurement of $24.2^{+1.7}_{-0.7}$ degrees even higher than Ma's individual measurement of the arms.

6.2. *Pitch Angle - SMBH Relation*

Strong evidence suggests that SMBHs reside in the nuclei of most galaxies (Kormendy & Richstone 1995; Kormendy & Gebhardt 2001). Additionally, it has recently been shown that a correlation exists between the pitch angle of spiral arms and SMBH mass in disc galaxies (Seigar et al. 2008). The relation is such that more massive SMBHs reside in galaxies with low pitch angle spiral arms (i.e., those that are tightly wound) and the least massive SMBHs are found in galaxies with high pitch angle spiral arms. Given that a significant fraction of galaxies in the Universe have spiral or barred spiral morphologies (Buta 1989), we wish to improve upon existing methods for measuring spiral arm pitch angle in order to quantify their structure. This measure can in turn be used to estimate the central black hole mass.

One of the current widely used relationships to SMBH mass is stellar velocity dispersion of the bulge/spheroid (Gebhardt et al. 2000a; Ferrarese & Merritt 2000). This technique requires spectroscopy of the galactic nucleus. Pitch angle determination only requires optical imag-
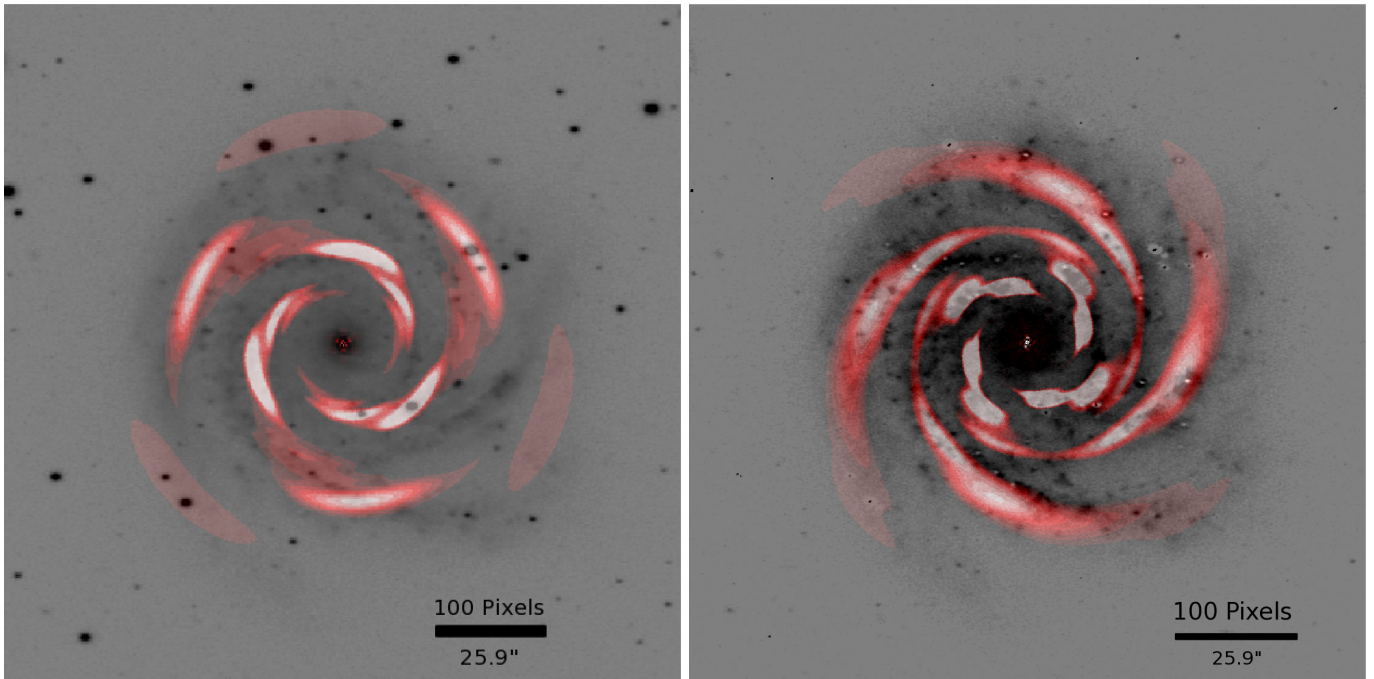
FIG. 20.— *Fig. 20a (left)* - Deprojected ($PA = 50°$ & $\alpha = 39.65°$) B-band inverse image of IC 4538, before star subtraction, overlaid with the contours of the Inverse FFT for the $m = 3$ harmonic mode (in red), conducted with an inner radius of 54 pixels ($14.0''$) and an outer radius of 258 pixels ($66.8''$), demonstrating a pitch angle of $-19.98°$. The contours are the real part of the complex spatial function of Equation 9 with $m = 3$. The contours illustrate the different levels of amplitude for the $m = 3$ harmonic mode. The overlaid Inverse FFT tends to track the bright foreground stars. *Fig. 20b (right)* - Star-subtracted and deprojected (with the same parameters as Fig. 20a) B-band inverse image of IC 4538, overlaid with the contours of the Inverse FFT for the $m = 4$ harmonic mode (in red), conducted with an inner radius of 54 pixels ($14.0''$) and an outer radius of 264 pixels ($68.4''$), demonstrating a pitch angle of $-15.42°$. The contours are the real part of the complex spatial function of Equation 9 with $m = 4$. The contours illustrate the different levels of amplitude for the $m = 4$ harmonic mode. In the absence of bright foreground stars, all four visible arms of the galaxy are tracked by the Inverse FFT overlay.
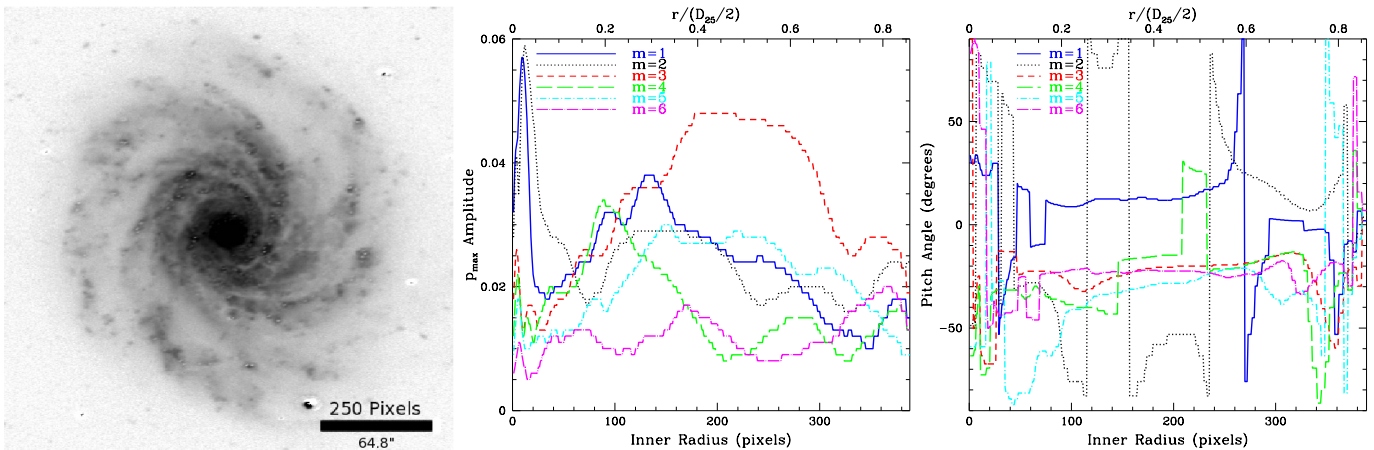

FIG. 21.— *Fig. 21a (left)* - Star-subtracted and deprojected ($PA = 5°$ & $\alpha = 53.84°$) B-band inverse image NGC 7083. *Fig. 21b (middle)* - Plot of the amplitude of p_{max} as a function of inner radius for NGC 7083, indicating the $m = 3$ component as the dominant harmonic mode for the galaxy. The $m = 3$ harmonic mode is dominant from an inner radius of 145 to 384 pixels ($37.6''$ to $99.5''$), constituting about 61% of the galaxy's radius. *Fig. 21c (right)* - A stable mean pitch angle of $-19.44°$ is determined for the $m = 3$ harmonic mode from a minimum inner radius of 143 pixels ($37.0''$) to a maximum inner radius of 319 pixels ($82.6''$), with an outer radius of 390 pixels ($101''$). This stretch of 176 pixels ($45.6''$) occupies 45% of the galactic disc. Equation 7 yields $E_\phi = 3.21°$ with $\lambda = 176$ pixels ($45.6''$), $\beta = 208$ pixels ($53.9''$), $\sigma = 2.67°$, and $\epsilon_3 = 0.58°$. The final determination of pitch angle is therefore $-19.44° \pm 3.21°$.
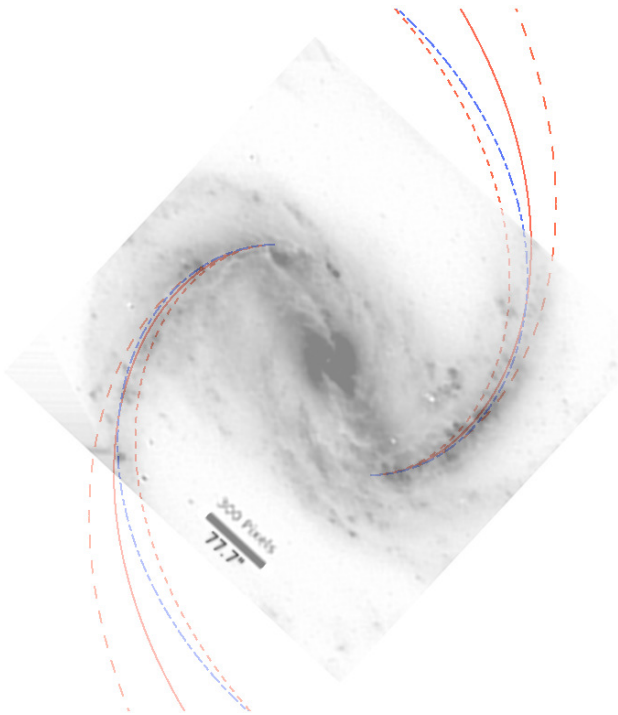
F<small>IG.</small> 22.— NGC 1365 (see Figure 12a) overlaid with a $m = 2$ spiral with $\phi = -34.81°$ (solid red lines) representing our best-fit pitch angle measurement (see Figure 12b), $\phi = -32.01°$ (short dashed red lines) representing our lower limit fit, $\phi = -37.61°$ (long dashed red lines) representing our upper limit fit, and $\phi = -16.5°$ (alternating short-long dashed blue lines) representing the average fit of Ma (2001) and Kennicutt (1981).

ing. Compared to simple optical imaging, which is widely and readily available, spectroscopy is time intensive. Other methods such as Reverberation Mapping (Gebhardt et al. 2000b) require long-term campaigns to obtain multi-epoch spectra and require significant telescope time and allocation. Even black hole estimates from single-epoch spectra (Vestergaard 2002) require spectroscopy. Other techniques such as bulge luminosity estimates (Kormendy 1993; Kormendy & Richstone 1995; Magorrian et al. 1998; Marconi & Hunt 2003; Häring & Rix 2004) require bulge decomposition. One specific bulge luminosity estimate incorporates Sérsic Index (Sérsic 1963) measurements of elliptical galaxies and the bulges of disc galaxies and relates them to SMBH mass (Graham & Driver 2007).

6.3. *Evolution of Pitch Angle with Redshift*

No matter how a logarithmic spiral is scaled, pitch angle is unaffected. This allows pitch angle measurements for distant galaxies to be considered equally valid as those for local galaxies. For distant galaxies, as long as spiral arms are detectable, it is possible to measure a pitch angle. Unlike other methods, details such as distance, extinction, etc. do not need to be known in order to measure pitch angle. Additionally, the measurement of pitch angle is independent of cosmological assumptions.

Upon examining the GOODS (Great Observatories Origins Deep Survey; Dickinson et al. 2003) fields, we have identified 224 spiral galaxies with spectroscopic (Barger et al. 2008) and photometric (Wolf et al. 2004) redshift (z) data for GOODS North and South, respectively. Of these 224 spiral galaxies, 179 galaxies lie in the range $z \leq 1$, 43 galaxies in the range $1 < z \leq 2$, and two galaxies with redshift greater than $z = 2$. So far, we have measured their pitch angles using the previous version of *2DFFT* and are planning on remeasuring the sample using the new iterative version of the code. This work demonstrates that it is not uncommon to be able to measure pitch angle for galaxies beyond a redshift of one. Current work also includes artificially redshifting (Barden et al. 2008) this GOODS sample of spiral galaxies in order to test the completeness of the GOODS fields (Shields 2012). Artificial redshifting allows us to predict at what distance spiral arms are no longer visible and thus pitch angle is immeasurable. Results thus far show no indications of a relationship between pitch angle and redshift (Shields et al. 2010), but this matter will be further explored.

6.4. *Continuing Efforts*

It is encouraging to notice increasing interest in the measurement of galactic spiral arm pitch angle in the astronomical community, as evidenced even in this past year (Kendall et al. 2011; Martínez-García 2012). Recent involvement from the computer science community has also been initiated with the use of computer vision techniques to measure galactic spiral arm pitch angle (Davis & Hayes 2012). We feel that our modification to the previously established Fourier methods for measuring galactic spiral arm pitch angle is a marked improvement and helps to satisfy a growing demand for its rapid and accurate measurement. Furthermore, we are glad to make the code publicly available to the benefit of anyone interested in furthering a much-needed exploration of spiral galaxy structure.

REFERENCES

Athanassoula, E., Romero-Gómez, M., Bosma, A., & Masdemont,
    J. J. 2009a, MNRAS, 400, 1706
—. 2010, MNRAS, 407, 1433
Athanassoula, E., Romero-Gómez, M., & Masdemont, J. J.
    2009b, MNRAS, 394, 67
Barden, M., Jahnke, K., & Häußler, B. 2008, ApJS, 175, 105
Barger, A. J., Cowie, L. L., & Wang, W. 2008, ApJ, 689, 687
Bertin, E. & Arnouts, S. 1996, A&AS, 117, 393
Block, D. L., Puerari, I., Frogel, J. A., Eskridge, P. B., Stockton,
    A., & Fuchs, B. 1999, Ap&SS, 269, 5
Buta, R. 1989, in The World of Galaxies (Le Monde des
    Galaxies), ed. H. G. Corwin Jr. & L. Bottinelli (New York:
    Springer-Verlag), 29–44
Considere, S. & Athanassoula, E. 1988, A&AS, 76, 365
Davis, D. R. & Hayes, W. B. 2012, in Computer Vision and
    Pattern Recognition (CVPR), 2012 IEEE Conference on, IEEE
de Vaucouleurs, G., de Vaucouleurs, A., Corwin, Jr., H. G., Buta,
    R. J., Paturel, G., & Fouque, P. 1991, Third Reference
    Catalogue of Bright Galaxies, ed. Roman, N. G., de
    Vaucouleurs, G., de Vaucouleurs, A., Corwin, H. G., Jr., Buta,
    R. J., Paturel, G., & Fouqué, P., Vol. 1-3 (Berlin, Heideleberg,
    and New York: Springer-Verlag), 2069
Dickinson, M., Giavalisco, M., & GOODS Team. 2003, in The
    Mass of Galaxies at Low and High Redshift, ed. R. Bender &
    A. Renzini (New York: Springer-Verlag), 324–331
Elmegreen, B. G., Elmegreen, D. M., & Montenegro, L. 1992,
    ApJS, 79, 37
Elmegreen, D. M. 1981, ApJS, 47, 229
Elmegreen, D. M. & Elmegreen, B. G. 1987, ApJ, 314, 3
Eskridge, P. B., Frogel, J. A., Pogge, R. W., Quillen, A. C.,
    Berlind, A. A., Davies, R. L., DePoy, D. L., Gilbert, K. M.,
    Houdashelt, M. L., Kuchinski, L. E., Ramírez, S. V., Sellgren,
    K., Stutz, A., Terndrup, D. M., & Tiede, G. P. 2002, ApJS,
    143, 73
Ferrarese, L. & Merritt, D. 2000, ApJ, 539, L9
Gebhardt, K., Bender, R., Bower, G., Dressler, A., Faber, S. M.,
    Filippenko, A. V., Green, R., Grillmair, C., Ho, L. C.,
    Kormendy, J., Lauer, T. R., Magorrian, J., Pinkney, J.,
    Richstone, D., & Tremaine, S. 2000a, ApJ, 539, L13
Gebhardt, K., Kormendy, J., Ho, L. C., Bender, R., Bower, G.,
    Dressler, A., Faber, S. M., Filippenko, A. V., Green, R.,
    Grillmair, C., Lauer, T. R., Magorrian, J., Pinkney, J.,
    Richstone, D., & Tremaine, S. 2000b, ApJ, 543, L5
Graham, A. W. & Driver, S. P. 2007, ApJ, 655, 77
Grosbol, P. J. & Patsis, P. A. 1998, A&A, 336, 840
Häring, N. & Rix, H. 2004, ApJ, 604, L89
Herschel, Sir, J. F. W. 1859, Outlines of Astronomy., ed.
    Herschel, J. F. W., Sir (London: Longman, Green, Longman,
    and Roberts, 6th ed.)
Ho, L. C., Li, Z.-Y., Barth, A. J., Seigar, M. S., & Peng, C. Y.
    2011, ApJS, 197, 21
Hozumi, S. 2003, in Lecture Notes in Physics, Berlin Springer
    Verlag, Vol. 626, Galaxies and Chaos, ed. G. Contopoulos &
    N. Voglis, 380–386
Jedrzejewski, R. I. 1987, MNRAS, 226, 747
Kendall, S., Kennicutt, R. C., & Clarke, C. 2011, MNRAS, 414,
    538
Kennicutt, Jr., R. C. 1981, AJ, 86, 1847
Kormendy, J. 1993, in IAU Symposium, Vol. 153, Galactic
    Bulges, ed. H. Dejonghe & H. J. Habing, 209—+
Kormendy, J. & Gebhardt, K. 2001, in American Institute of
    Physics Conference Series, Vol. 586, 20th Texas Symposium on
    relativistic astrophysics, ed. J. C. Wheeler & H. Martel,
    363–381
Kormendy, J. & Richstone, D. 1995, ARA&A, 33, 581
Lin, C. C. & Shu, F. H. 1964, ApJ, 140, 646
Lintott, C. J., Schawinski, K., Slosar, A., Land, K., Bamford, S.,
    Thomas, D., Raddick, M. J., Nichol, R. C., Szalay, A.,
    Andreescu, D., Murray, P., & Vandenberg, J. 2008, MNRAS,
    389, 1179
Ma, J. 2001, Chinese J. Astron. Astrophys., 1, 395
Magorrian, J., Tremaine, S., Richstone, D., Bender, R., Bower,
    G., Dressler, A., Faber, S. M., Gebhardt, K., Green, R.,
    Grillmair, C., Kormendy, J., & Lauer, T. 1998, AJ, 115, 2285
Marconi, A. & Hunt, L. K. 2003, ApJ, 589, L21
Martínez-García, E. E. 2012, ApJ, 744, 92
Moore, B., Katz, N., Lake, G., Dressler, A., & Oemler, A. 1996,
    Nature, 379, 613
Press, W. H., Flannery, B. P., Teukolsky, S. A., & Vetterling,
    W. T. 1989, Numerical recipes in C. The Art of Scientific
    Computing, ed. Press, W. H., Flannery, B. P., Teukolsky, S. A.,
    & Vetterling, W. T. (Cambridge: University Press.)
Puerari, I., Block, D. L., Elmegreen, B. G., Frogel, J. A., &
    Eskridge, P. B. 2000, A&A, 359, 932
Puerari, I. & Dottori, H. A. 1992, A&AS, 93, 469
Purcell, C. W., Bullock, J. S., Tollerud, E. J., Rocha, M., &
    Chakrabarti, S. 2011, Nature, 477, 301
Ringermacher, H. I. & Mead, L. R. 2009, MNRAS, 397, 164
Roberts, W. W. 1969, ApJ, 158, 123
Saraiva Schroeder, M. F., Pastoriza, M. G., Kepler, S. O., &
    Puerari, I. 1994, A&AS, 108, 41
Savchenko, S. S. & Reshetnikov, V. P. 2011, Astronomy Letters,
    37, 817
Seiden, P. E. & Gerola, H. 1982, Fund. Cosmic Phys., 7, 241
Seigar, M. S., Block, D. L., Puerari, I., Chorney, N. E., & James,
    P. A. 2005, MNRAS, 359, 1065
Seigar, M. S., Bullock, J. S., Barth, A. J., & Ho, L. C. 2006, ApJ,
    645, 1012
Seigar, M. S. & James, P. A. 1998, MNRAS, 299, 685
Seigar, M. S., Kennefick, D., Kennefick, J., & Lacy, C. H. S. 2008,
    ApJ, 678, L93
Sérsic, J. L. 1963, Boletin de la Asociacion Argentina de
    Astronomia La Plata Argentina, 6, 41
Shields, D. W. 2012, in Preparation
Shields, D. W., Hughes, J. A., Barrows, S. R., Davis, B.,
    Kennefick, D., Kennefick, J., Ring, W., & Seigar, M. 2010, in
    American Institute of Physics Conference Series, Vol. 1294,
    American Institute of Physics Conference Series, ed.
    D. J. Whalen, V. Bromm, & N. Yoshida, 283–284
Shu, F. H., Milione, V., Gebel, W., Yuan, C., Goldsmith, D. W.,
    & Roberts, W. W. 1972, ApJ, 173, 557
Thornley, M. D. 1996, ApJ, 469, L45+
Tody, D. 1986, in Presented at the Society of Photo-Optical
    Instrumentation Engineers (SPIE) Conference, Vol. 627,
    Society of Photo-Optical Instrumentation Engineers (SPIE)
    Conference Series, ed. D. L. Crawford, 733—+
Vestergaard, M. 2002, ApJ, 571, 733
Wolf, C., Meisenheimer, K., Kleinheinrich, M., Borch, A., Dye, S.,
    Gray, M., Wisotzki, L., Bell, E. F., Rix, H., Cimatti, A.,
    Hasinger, G., & Szokoly, G. 2004, A&A, 421, 913

TABLE 3
PITCH ANGLE LITERATURE COMPARISON

Galaxy	This Work m	φ	Band	Source	Ref. 1 m	Ref. 1 φ (deg.)	Ref. 2 φ (deg.)	Ref. 3 φ (deg.)	Ref. 4 φ (deg.)	Ref. 4 Band	Ref. 5 φ (deg.)
M51a	2	16.26 ± 3.20	B	3	⋯	⋯	14	16.7, 15.8	⋯	⋯	15 ± 2
NGC 150	2	14.29 ± 4.26	B	1	2	$17.6^{+1.3}_{-2.0}$	⋯	35.0	⋯	⋯	⋯
NGC 157	3	8.66 ± 0.89	B	1	⋯	⋯	⋯	⋯	⋯	⋯	19 ± 4
NGC 210	2	−15.81 ± 3.25	B	1	2	$15.7^{+0.5}_{-0.5}$	⋯	⋯	⋯	⋯	11 ± 2
NGC 289	5	19.71 ± 1.95	B	1	2	$17.2^{+1.3}_{-1.8}$	⋯	⋯	⋯	⋯	11 ± 2
NGC 578	3	16.51 ± 1.88	B	1	2	$23.0^{+0.9}_{-1.3}$	⋯	⋯	⋯	⋯	⋯
NGC 598	2	−33.90 ± 5.72	6450 Å[a]	2	⋯	⋯	⋯	⋯	⋯	⋯	31 ± 5
NGC 895	2	−38.50 ± 4.77	I	1	⋯	⋯	⋯	⋯	⋯	⋯	22 ± 3
NGC 1042	4	39.50 ± 4.48	R	1	⋯	⋯	⋯	⋯	⋯	⋯	13 ± 3
NGC 1097[b]	2	15.80 ± 3.62	I	1	⋯	⋯	⋯	10.6	⋯	⋯	17 ± 4
NGC 1187	4	−21.96 ± 3.61	B	1	2	$19.4^{+1.1}_{-1.0}$	⋯	⋯	⋯	⋯	14 ± 4
NGC 1232	3	−25.71 ± 5.43	B	1	⋯	⋯	⋯	⋯	⋯	⋯	15 ± 4
NGC 1300	2	−12.71 ± 1.99	B	1	2	$13.1^{+7.7}_{-0.3}$	⋯	12.1, 11.0	⋯	⋯	⋯
NGC 1365	2	−34.81 ± 2.80	B	1	⋯	⋯	⋯	13.8, 17.8	⋯	⋯	18 ± 3
NGC 1398	4	19.61 ± 3.07	V	1	⋯	⋯	⋯	⋯	⋯	⋯	6 ± 2
NGC 1566	2	−17.81 ± 3.67	B	1	⋯	⋯	20	19.1, 14.0	⋯	⋯	22 ± 2
NGC 2442	2	14.95 ± 4.20	V	1	⋯	⋯	⋯	⋯	⋯	⋯	28 ± 3
NGC 2835	3	−23.97 ± 2.22	B	1	⋯	⋯	⋯	⋯	⋯	⋯	20 ± 2
NGC 3198	2	18.20 ± 10.01	R	3	⋯	⋯	15	⋯	⋯	⋯	⋯
NGC 3223	4	−10.92 ± 2.17	B	1	⋯	⋯	⋯	⋯	−8.7 ± 0.5	B	⋯
NGC 3261	6	15.38 ± 0.71	B	1	1	$10.2^{+20.1}$	⋯	⋯	⋯	⋯	13 ± 2
NGC 3513	1	5.84 ± 1.46	B	1	2	$24.2^{+1.7}_{-0.7}$	⋯	18.2, 8.1	⋯	⋯	⋯
NGC 3783	2	10.71 ± 0.64	B	1	⋯	⋯	⋯	⋯	⋯	⋯	7 ± 1
NGC 3938	3	−22.37 ± 7.21	B	3	⋯	⋯	15	⋯	⋯	⋯	12 ± 3
NGC 4030	3	23.48 ± 5.76	B	1	⋯	⋯	⋯	⋯	⋯	⋯	12 ± 2
NGC 4321	5	21.81 ± 3.57	R	3	⋯	⋯	20	21.0, 14.3	⋯	⋯	15 ± 3
NGC 4930	3	30.29 ± 3.45	B	1	1	$13.9^{+0.9}_{-2.0}$	⋯	⋯	⋯	⋯	⋯
NGC 4939	6	11.48 ± 1.71	B	1	⋯	⋯	⋯	8.1, 10.8	⋯	⋯	11 ± 2
NGC 4995	2	13.00 ± 2.88	B	1	2	$78.3^{+5.4}_{-8.3}$	⋯	⋯	⋯	⋯	⋯
NGC 5085	2	−11.32 ± 1.77	4680 Å[c]	4	⋯	⋯	⋯	⋯	−10.9 ± 0.5	B	12 ± 2
NGC 5236	6	−16.04 ± 1.74	B	1	⋯	⋯	⋯	⋯	⋯	⋯	16 ± 2
NGC 5247	2	−31.94 ± 5.75	B	1	⋯	⋯	⋯	⋯	−27.4 ± 0.7	B	28 ± 4
NGC 5483	2	−22.98 ± 4.52	B	1	2	$21.6^{+1.4}_{-0.9}$	⋯	⋯	⋯	⋯	⋯
NGC 5861	2	−14.91 ± 0.83	V	1	⋯	⋯	⋯	13.6, 12.7	−11.9 ± 0.5	V	⋯
NGC 6221	6	−27.18 ± 2.14	B	1	2	$19.9^{+1.6}_{-0.7}$	⋯	⋯	⋯	⋯	⋯
NGC 6300	4	−16.58 ± 1.52	B	1	2	$20.3^{+0.6}_{-1.1}$	⋯	⋯	−15.0 ± 1.0	B	⋯
NGC 7083	3	−19.44 ± 3.21	B	1	⋯	⋯	⋯	⋯	⋯	⋯	⋯
NGC 7793	2	13.91 ± 4.40	B	1	⋯	⋯	16	⋯	⋯	⋯	⋯

NOTE. — Col. (1) galaxy name; col. (2) dominant harmonic mode found by this work; col. (3) pitch angle from this work; col. (4) waveband/wavelength used by this work; col. (5) telescope/survey imaging source used by this work; col. (6) "Fourier Method" harmonic mode used by Martínez-García (2012); col. (7) B-band "Fourier Method" pitch angle absolute value from Martínez-García (2012); col. (8) NIR and optical average $m = 2$ pitch angle absolute value from Kendall et al. (2011); col. (9) B-band pitch angle absolute value for individual arms from Ma (2001); col. (10) $m = 2$ pitch angle from Grosbol & Patsis (1998); col. (11) waveband used by Grosbol & Patsis (1998); and col. (12) $H\alpha$ $m = 2$ pitch angle absolute value from Kennicutt (1981). Source (1) CGS; source (2) Palomar 48 inch Schmidt; source (3) KPNO 2.1 m CFIM; and source (4) UK 48 inch Schmidt. Ref. (1) Martínez-García (2012); ref. (2) Kendall et al. (2011); ref. (3) Ma (2001); ref. (4) Grosbol & Patsis (1998); and ref. (5) Kennicutt (1981).

[a] 103aE emulsion.

[b] In addition to spiral arms in the disc of the galaxy, NGC 1097 displays rare $m = 2$ nuclear spiral arms in the bulge. These arms display an opposite chirality to the disc arms with $\phi = -30.60° \pm 2.68°$.

[c] IIIaJ emulsion.